N O T I C E

CORNELL UNIVERSITY

Center for Radiophysics and Space Research

ITHACA, N. Y.

STELLAR CONVECTION III:

CONVECTION AT LARGE RAYLEIGH NUMBERS

Philip S. Marcus

STELLAR CONVECTION III:

CONVECTION AT LARGE RAYLEIGH NUMBERS

Philip S. Marcus[*]

Center for Radiophysics and Space Research

Cornell University

November 1979

ABSTRACT

We present the results of a numerical, 3-dimensional study of convection in a self-gravitating sphere of Boussinesq fluid with a Rayleigh number of 10^{10} and a Prandtl of 1. The velocity and temperature are computed by using spectral methods (spherical harmonics, $Y^{\ell,m}$ $\ell \leq 12$) in the horizontal and finite-differencing in the radial directions. An eddy viscosity and diffusivity are needed to model the sub-resolution flow. The amplitudes of the eddy viscosity and diffusivity are determined by requiring that the time-averaged kinetic and thermal energy spectra remain unchanged when the limit of spatial resolution varies. For Rayleigh numbers much less than 10^{10} the flows do not have well-defined inertial ranges and an eddy viscosity and diffusivity cannot be assigned in this self-consistent manner. By computing the energy spectra as well as the detailed energy budgets as a function of wavenumber, we show that for $R_s = 10^{10}$ there is an inertial range for the modes corresponding to spherical harmonics with $\ell > 6$. We also show that the velocity field becomes nearly isotropic at small wavelengths. Intermittent bursts of convective flux and energy propagate inward from the outer boundary-layer. The bursts are shown to cascade from large to small wavelengths.

Subject headings: convection - stars: interiors - hydrodynamics

I. INTRODUCTION

This is the third in a series of papers on convection in
spheres. In it we extend our numerical calculations to high Ray-
leigh numbers. In the second paper of this series, the Rey-
nolds and Peclet numbers were small enough so that the small length-
scales where dissipation occurs could be resolved. In this paper
the dissipative lengthscales are much smaller than the numerical
resolution, so it is necessary to model the small wavelength end
of the kinetic and thermal energy spectra. Clearly, no attempt
to compute the convective flows in the cores of stars (where the
Reynolds numbers are greater than 10^{10}) is able to resolve
all of the scales of motion so it is necessary to model the
unresolved part of the flow. For example, the mixing-length treat-
ment of convection and the spectral method proposed by Ledoux et al.
(1961) both assume that buoyancy drives the convection in a narrow
band of large wavelength modes. Both methods utilize the
model of homogeneous, isotropic turbulence in which buoyancy is
not important to compute the effects of the small-scale unresolved
motions.

In an actual sphere of convecting fluid we might expect that
the buoyancy effects are felt over a wide range of wavelengths, and
that the fluid which is strongly driven by the buoyancy in the
radial direction is neither uniform nor isotropic for an even
wider range of wavelengths. In this paper we explicitly compute
the fluid's velocity and temperature at the largest wavelengths
and confirm that the fluid is anisotropic and that
the energy spectra are not smooth functions of wavelength but

have a large amount of fine structure. At smaller wavelengths
we also   compute the flow and show that it becomes
isotropic and that   the energy spectra develop inertial ranges
with the smooth $\sim k^{-5/3}$ power law associated with homogeneous
turbulence. We are then able to model the effects of the small
scale fluid motions by assuming that the calculated intertial range
smoothly continues beyond our limit of spatial resolution. In §2
we show how to parameterize the transport properties of the unre-
solvable inertial subrange with eddy viscosities and diffusivities.
The time-averaged results of our calculations are presented in §3.
In the fourth section we examine the time-dependent fluctuations
in the energy spectra and show how they cascade from large to small
wavelengths. A summary of our conclusions appears in §5.

II. EDDY VISCOSITY AND DIFFUSIVITY

A) Motivation

Unfortunately, it is impossible to compute numerical solutions to the Navier-Stokes equation for large Reynolds number flows. The Reynolds number in the convective core of an O star is $\sim 10^{12}$, which means that the ratio of the pressure scale-height to the dissipative length-scale is $\sim 10^9$. Unless a numerical method has the capability of resolving this range of scales, the resulting solution will lack some essential physics. To circumvent their inability to resolve the dissipative scales, hydrodynamicists typically model the dissipation by replacing the true kinetic viscosity, ν, with an eddy viscosity, ν_e, with $\nu_e \gg \nu$. It is usually argued (c.f. Deardorff, 1972 and references therein) from dimensional analysis that ν_e should be of the form

$$\nu_e = c \, L_{res} \, V_{res} \tag{2.1}$$

where L_{res} and V_{res} are the length and velocity at the limit of the spatial resolution and c is a constant of order unity that is independent of both position and L_{res}. Similar reasoning shows that an eddy diffusivity, $\hbar_e$, of the same form as equation (2.1) should be included in the heat diffusion equation. More complicated models for eddy viscosities exist (c.f. Kraichnan, 1976). However, a simple test of the validity of an eddy viscosity of the form of equation (2.1) is to see if we can find a value of c (independent of a position) such that all solutions computed with this value of c, but with different limits of spatial resolution, have the same energy spectra. This type of test is easily performed

with a modal analysis.

B) Definitions and Their Implications

Let the temperature T be a sum of its resolvable $\hat{T}$ and unresolvable T' parts. If we assume that the radial resolution is much greater than the angular resolution, then we may write

$$\hat{T} = \sum_{\ell=0}^{\ell_{cutoff}} \sum_{m,\gamma} T_{\gamma,\ell,m}(r,t) \, Y^{\gamma,\ell,m} = \sum_{\ell=0}^{\ell_{cutoff}} T_\ell \qquad (2.2)$$

and

$$T' = \sum_{\ell=\ell_{cutoff}+1}^{\infty} \sum_{m,\gamma} T_{\gamma,\ell,m}(r,t) \, Y^{\gamma,\ell,m} = \sum_{\ell=\ell_{cutoff}+1}^{\infty} T_\ell \qquad (2.3)$$

The sums in equation (2.2) - (2.3) are over $0 \leq m \leq \ell$ with γ equal to R and I, where

$$Y^{R,\ell,m} \equiv \begin{cases} 2(2\pi)^{1/2} \, \mathrm{Re}\,(Y^{\ell,m}) & m \neq 0 \\ 2(\pi)^{1/2} \, Y^{\ell,o} & m = 0 \end{cases} \qquad (2.4)$$

$$Y^{I,\ell,m} \equiv \begin{cases} 2(2\pi)^{1/2} \, \mathrm{Im}\,(Y^{\ell,m}) & m \neq 0 \\ 0 & m = 0 \end{cases} \qquad (2.5)$$

and where $\mathrm{Re}\,(Y^{\ell,m})$ and $\mathrm{Im}(Y^{\ell,m})$ are the real and imaginary parts of the spherical harmonic. We use the notation throughout that any quantity written with subscripts γ,ℓ,m is a function only of radius and time and corresponds to the (γ,ℓ,m) component of a quantity, i.e.,

$$f_{\gamma,\ell,m}(r,t) \equiv \frac{1}{4\pi} \int_{4\pi} Y^{\gamma,\ell,m} \, f(r,\theta,\phi,t) \, d\Omega \qquad (2.6)$$

Writing $\underline{v} = \hat{v} + v'$, we can define an eddy diffusivity for each mode, $\mathcal{R}_e^{\gamma,\ell,m}(\ell_{cutoff}, r, t)$ such that

$$\nabla \cdot [\mathcal{R}_e^{\gamma,\ell,m} \nabla(\hat{T}_{\gamma,\ell,m} Y^{\gamma,\ell,m})] - [(\hat{\underline{v}}\cdot\nabla)\hat{T}]_{\gamma,\ell,m} Y^{\gamma,\ell,m}$$
$$\equiv - [(\underline{v}\cdot\nabla) T_{\gamma,\ell,m} Y^{\gamma,\ell,m}] \tag{2.7}$$

All of the quantities on the left-hand side of equation (2.7) are numerically calculable except for $\mathcal{R}_e^{\gamma,\ell,m}$. If $\underline{v}$ and T were known over all scales, we could then solve for $\mathcal{R}_e^{\gamma,\ell,m}(\ell_{cutoff}, r, t)$ and determine how strongly it depends on γ, ℓ, m, r, t, and ℓ_{cutoff}. Similarly we can define two eddy viscosities for each (γ, ℓ, m) component of the velocity. There are two viscosities because the velocity has two degrees of freedom.

The toroidal eddy viscosity, $\nu_T^{\gamma,\ell,m}(\ell_{cutoff}, r, t)$, is defined:

$$\hat{e}_r \cdot \{\nabla \times [(\hat{\underline{v}}\cdot\nabla)\hat{\underline{v}} - (\underline{v}-\nabla)\underline{v}]\}_{\gamma,\ell,m} = \hat{e}_r \{\nabla\times[\nabla\cdot(\nu_T^{\gamma,\ell,m}\nabla\hat{\underline{v}}]_{\gamma,\ell,m} \tag{2.8}$$

and the poloidal eddy viscosity, $\nu_p^{\gamma,\ell,m}(\ell_{cutoff}, r, t)$, by

$$\{[(\hat{\underline{v}}\cdot\nabla)\hat{\underline{v}} - (\underline{v}\cdot\nabla)\underline{v}] - \nabla P^{im}\}_{\gamma,\ell,m} = \hat{e}_r \cdot [\nabla\cdot(\nu_p^{\gamma,\ell,m}\nabla\underline{v})]\}_{\gamma,\ell,m} \tag{2.9}$$

The pressure, P^{im}, that appears in equation (2.9) is the part of the resolvable pressure that is due to nonlinear terms involving $\underline{v}'$:

$$\nabla^2 (P^{im}_{\gamma,\ell,m} Y^{\gamma,\ell,m}) = -\{\nabla\cdot [(\underline{v}\cdot\nabla)\underline{v} - (\hat{\underline{v}}\cdot\nabla)\hat{\underline{v}}]\}_{\gamma,\ell,m} Y^{\gamma,\ell,m} \tag{2.10}$$

It is necessary to include P^{im} in equation (2.8) to make $[(\underline{v}\cdot\nabla)\underline{v} - (\underline{v}\cdot\nabla)\underline{v} - \nabla P^{im}]$ divergenceless. The resolvable pressure $\hat{P}_{\gamma,\ell,m}$ is then equal to

$$\hat{P}_{\gamma,\ell,m} = P^{ex}_{\gamma,\ell,m} + P^{im}_{\gamma,\ell,m} \qquad (2.11)$$

where

$$\nabla^2(P^{ex}_{\gamma,\ell,m}Y^{\gamma,\ell,m}) = -\{\nabla\cdot[(\hat{\underline{v}}\cdot\nabla)\hat{\underline{v}}]\}_{\gamma,\ell,m}\, Y^{\gamma,\ell,m}$$

$$+ r^{-2}R_sP_r\, \partial(r^3\hat{T}_{\gamma,\ell,m})/\partial r\, Y^{\gamma,\ell,m} \qquad (2.12)$$

Equations (2.8) and (2.9) provide a complete description for the resolvable part of $[(\hat{\underline{v}}\cdot\underline{\nabla})\hat{\underline{v}} - (\underline{v}\cdot\nabla)\underline{v} - \nabla P^{im}]$:

$$[(\hat{\underline{v}}\cdot\nabla)\hat{\underline{v}} - (\underline{v}\cdot\nabla)\underline{v} - \nabla P^{im}] =$$

$$\sum_{\gamma,\ell,m}[\ell(\ell+1)]^{-1}\, \{\nabla\partial[r^2\hat{e}_r\cdot\nabla(\nu_p^{\gamma,\ell,m}\nabla\hat{\underline{v}})]/\partial r$$

$$- r\,\nabla^2[r^2\hat{e}_r\cdot\nabla\cdot(\nu_p^{\gamma,\ell,m}\nabla\hat{\underline{v}})]\,\hat{e}_r$$

$$- \hat{e}_r\times\nabla\,[r^2\hat{e}_r\cdot\{\nabla\times[\nabla\cdot(\nu_T^{\gamma,\ell,m}\nabla\hat{\underline{v}})]\}\} \qquad (2.13)$$

If $\nu^T=\nu^P$ one might conclude from equations (2.8) and (2.9) that $[(\hat{\underline{v}}\cdot\nabla)\hat{\underline{v}} - (\underline{v}\cdot\nabla)\underline{v} - \nabla P^{im}]$ is equal to $\nabla\cdot(\nu_p\nabla\hat{\underline{v}})$, but this is not

true because the latter quantity is not divergenceless. When modeling $\underline{v}'$ with an eddy viscosity, one must be careful that the model is realizable; that is $(\underline{v}')^2$ should never be negative. This problem is frequently encountered (c.f. Schlesinger, 1978) but does not occur in our modal definitions of eddy viscosity.

For the eddy viscosities and diffusivity to be numerically useful tools, they must be independent of γ and m. At large wave-numbers, we expect the temperature and velocity to be isotropic. Furthermore, if the nonlinear terms are dominated by local inter-actions in phase space {i.e. the interaction of $\underline{v}_{\gamma',\ell',m'}$ with $T_{\gamma'',\gamma'',m''}$ is an important contribution to $[(\underline{v}\cdot\nabla)T]_{\gamma,\ell,m}$ only if

$\ell' \simeq \ell'' \simeq \ell$} then we expect $\mathcal{R}_e{}^{\gamma,\ell,m}$ to be independent of γ and m for large values of ℓ. For small values of ℓ the flow is not isotropic and $\mathcal{R}_e{}^{\gamma,\ell,m}$ will not be independent of γ,m. However, if ℓ_{cutoff} is sufficiently large, then

$$|\nabla \cdot (\mathcal{R}_e{}^{\gamma,\ell,m}\nabla T)_{\gamma,\ell,m}| << |[(\underline{\hat{v}}\cdot\nabla)\hat{T}]_{\gamma,\ell,m}| \quad \text{for } \ell << \ell_{cutoff} \quad (2.14)$$

Therefore, small errors in eddy diffusivity caused by assuming that $\mathcal{R}_e{}^{\gamma,\ell,m}$ is independent of γ and m for low values of ℓ will be negligible in comparison to the explicitly calculated nonlinear advective terms.

Assuming that the eddy diffusivity and viscosities are independent of γ and m, we parameterize them as:

$$\mathcal{R}_e = 2\pi[\ell_{cutoff}(\ell_{cutoff}+1)]^{-1/2}[KE(\ell_{cutoff},r)/2\pi r^2]^{1/2} \, C_K$$
$$(2.15)$$

$$\nu_p = 2\pi[\ell_{cutoff}(\ell_{cutoff}+1)]^{-1/2}[KE(\ell_{cutoff},r)/2\pi r^2]^{1/2} \, C_p$$
$$(2.16)$$

$$\nu_T = 2\pi[\ell_{cutoff}(\ell_{cutoff}+1)]^{-1/2}[KE(\ell_{cutoff},r)/2\pi r^2]^{1/2} \, C_T$$
$$(2.17)$$

where $KE(\ell,r)$ is the kinetic energy of all modes with wavenumber ℓ at radius r (see Marcus 1980a, hereafter referred to as Paper II). The length and velocity at the resolution limit are taken to be $2\pi[\ell_{cutoff}(\ell_{cutoff}+1)]$ and $[KE(\ell_{cutoff},r)/2\pi r^2]^{1/2}$ respectively. The eddy coefficients C_p, C_T, and C_k are functions of ℓ, as well as r and t. However, if ℓ_{cutoff} lies in the self-similar inertial range, dimensional arguments can be used to show that C_K, C_T and C_p should be independent of ℓ. The gist of the argument is that the rate at which energy is transferred from modes of wavenumber

ℓ to modes with wavenumber greater than ℓ_{cutoff} is (Tennekees and Lumley 1972)

$$S(\ell)^2 \ E(\ell_{cutoff})/S(\ell_{cutoff}) \qquad (2.18)$$

where $S(\ell)$ is the strain and $E(\ell)$ is the energy associated with modes of wavenumber ℓ. If $\underline{v} \sim \ell^{-1/3}$ then $S \sim \ell^{2/3}$ and $E \sim \ell^{-2/3}$ so the rate is proportional to $(\ell/\ell_{cutoff})^{4/3}$. Using the eddy viscosity in the modal Navier-Stokes equation, this same dissipation rate is proportional to

$$\ell^2 \ E(\ell) \ \nu_p{}^{\gamma,\ell,m} = C_p \ (\ell/\ell_{cutoff})^{4/3} \qquad (2.19)$$

if $C_p \approx C_T$. Setting the two expressions for the rates equal, we see that C_p is independent of ℓ.

C) Self-Consistency and a Method of Solution

The most difficult task in implementing the eddy viscosity is choosing the values of C_p, C_T and C_K. They are usually chosen (Deardorff, 1972; Siggia, 1978) by varying their values until the resulting kinetic and thermal energy spectra have smooth, $k^{-5/3}$ power laws. This method is not only arbitrary but somewhat expensive in that several solutions with differing values of the eddy coefficients must be computed before the correct values of the eddy coefficients can be determined.

We shall establish the values of the eddy coefficients by appealing to the self-consistency requirement that C_p, C_T, and C_K are independent of ℓ_{cutoff}. Specifically, the time-averaged thermal energy, poloidal kinetic energy, and toroidal kinetic energy spectra should not change when ℓ_{cutoff} is changed

from 12 to 10. A necessary condition for the thermal energy spectra to be the same is that the rate at which the thermal energy cascades in and out of the modes with wavenumber ℓ due to the advective term is independent of ℓ_{cutoff}. The rate of this energy cascade is $\sum_{\gamma,m} \hat{T}_{\gamma,\ell,m}[(\underline{v}\cdot\nabla)T]_{\gamma,\ell,m}$. For the cascade rate with $\ell_{cutoff}=12$ to be equal to the rate with $\ell_{cutoff}=10$ requires that

$$\hat{T}_{\gamma,\ell,m} \nabla \cdot \{[\overset{\ell}{\mathcal{R}_e}{}^{\gamma,\ell,m}(12) - \overset{\ell}{\mathcal{R}_e}{}^{\gamma,\ell,m}(10)] \nabla \hat{T}\}_{\gamma,\ell,m} =$$

$$\hat{T}_{\gamma,\ell,m} \{\underline{v}\cdot\nabla [T_{11}+T_{12}] + [\underline{v}_{11}+\underline{v}_{12}]\cdot\nabla \hat{T} \quad (2.20)$$

$$+ [\underline{v}_{11}+\underline{v}_{12}] \cdot\nabla [T_{11}+T_{12}]\}_{\gamma,\ell,m}$$

where $\overset{\ell}{\mathcal{R}_e}{}^{\gamma,\ell,m}(12)$ and $\overset{\ell}{\mathcal{R}_e}{}^{\gamma,\ell,m}(10)$ are calculated from eq.(2.15) using ℓ_{cutoff} equal to 12 and 10 respectively and where $\hat{T}$ and $\underline{\hat{v}}$ are the resolvable temperature and velocity with $\ell_{cutoff}=10$. Using equation (2.15) for $\overset{\ell}{\mathcal{R}_e}{}^{\gamma,\ell,m}$ in equation (2.20) we obtain a linear differential equation for C_K (r) which may be numerically solved:

$$C_K[A(r) \sum_{\gamma,m} T_{\gamma,\ell,m} \mathcal{D}_\ell T_{\gamma,\ell,m} + \frac{1}{2} \partial A/\partial r \; \partial T^2_{\gamma,\ell,m}/\partial r]$$

$$+ \frac{1}{2} \frac{\partial C_K}{\partial r} A(r) \sum_{\gamma,m} \partial T^2_{\gamma,\ell,m}/\partial r = \quad (2.21)$$

$$\sum_{\gamma,m} T_{\gamma,\ell,m}[\underline{\hat{v}}\cdot\nabla(T_{11} + T_{12}) + (\underline{v}_{11} + \underline{v}_{12})\cdot\nabla(\hat{T} + T_{11} + T_{12})]_{\gamma,\ell,m};$$

where

$$A(r) \equiv (2\pi)^{1/2} r^{-1}[(12\cdot13)^{-1/2} KE(12,r)^{1/2} - (10\cdot11) KE(10,r)^{1/2}]$$

$$(2.22)$$

and where $\mathcal{D}_\ell$ is the 2-dimensional Laplacian, $\mathcal{D}_\ell \equiv (\nabla^2 - 1/r\partial^2/\partial r^2 r)$.

Now, C_K obtained from equation (2.21) will obviously be a function of r. Also, we can obtain different values of C_K by choosing a different value of ℓ in equation (2.21) or by choosing a different pair of values for ℓ_{cutoff}. It is a test of the self-consistency of our eddy diffusivity model if we can show that C_K does not vary much with radius or depend strongly on our choices of ℓ and ℓ_{cutoff}. By examining the kinetic energy budgets of the poloidal and toroidal velocity, we obtain differential equations similar to (2.21) for C_p and C_T.

An advantage of using equation (2.21) to compute C_K at each timestep is that the iterative values converge rapidly. To see the rapid convergence, let us assume that we have underestimated C_K. A small value of C_K makes the thermal energy extraordinarily large at the $\ell=11$ and $\ell=12$ wavenumbers since it is not dissipated and piles up near ℓ_{cutoff} (see Marcus 1980b). The upward curl of the energy spectrum makes the right-hand side of equation (2.21) large and thereby increases C_K. The convergence of the equations that govern C_p and C_T is even more rapid because it can be shown that C_p and C_T are nearly proportional to $1/A(r)$ or $1/\{[KE(10,r)]^{1/2}-.8397[KE(12,r)]^{1/2}\}$. If C_p or C_T is underestimated, the upward curl on the energy spectrum at $\ell=12$ causes this denominator to shrink, causing C_p and C_T to increase rapidly. Likewise, if C_p is too large, $KE(12,r)$ dissipates to zero, the denominator becomes large, and C_p decreases.

D) Numerical Results

We have integrated the modal equations of convection (Paper II) with the eddy viscosities and conductivity described in this section.

For a Prandtl number of 1 and a Rayleigh number less than 10^8, the values obtained for the eddy coefficients $C_p(r)$, $C_T(r)$ and $C_K(r)$ varied widely with radius, ℓ and pair of ℓ_{cutoff}'s. We have concluded that our model of the eddy viscosity is not valid in this regime. This result should not be surprising since the Reynolds numbers are less than 500 and the high wavenumber modes are neither isotropic nor   lie in an inertial range.

For a Rayleigh number of 10^{10} the eddy coefficients do converge. With ℓ_{cutoff} equal to 10 and 12 and ℓ equal to 8 in equation (2.20), the value of C_K changes by less than 15% from $r=0$ to $r=0.8$. The time-averaged value of C_p averaged over $0 \le r \le .8$ is 0.52. In the turbulent boundary-layer between $r=0.8$ and $r=1.0$, C_K is $\sim$ 20% lower than this value. The coefficients C_T and C_p are similarly well behaved with average values of 0.55 and 0.46 respectively. Using the velocity and temperature produced from these eddy coefficients in eq. (2.21) with $\ell=6$ and ℓ_{cutoff} equal to 10 and 8, we have computed a new averaged value of C_K that   is $\sim$ 10% lower than the old value. The decrease in eddy diffusivity is due to the fact that the calculated $\ell=6$ energies are higher (due to production) than we would have predicted by using the value of the thermal energy at $\ell = 12$ and extrapolating to $\ell = 6$ using a $k^{-5/3}$ spectrum (see §3). New average values of C_p and C_T were also computed based on $\ell = 6$ and $\ell_{cutoff} = 10$ and 8. The value of C_p was $\sim$ 10% lower, but C_T was $\sim$ 10% higher than its original value because the $\ell = 6$ toroidal kinetic energy is lower than we would have

predicted (assuming a $k^{-5/3}$ spectrum and knowing the value of
the toroidal kinetic energy at $\ell = 12$). The toroidal kinetic
energy is relatively low at low wavenumbers because it is not
produced at the low wavenumbers by buoyancy; it is produced
at the high wavenumbers by isotropization of the velocity.
The new values of C_p, C_T, and C_K, like the old values,
are only weakly ($\sim$12%) dependent upon radius. We have computed
the time-averaged eddy coefficients with 3 other possible combi-
nations of ℓ and ℓ_{cutoff} and find only a weak ($\sim$15%) dependence
on these values. Because the eddy coefficients are nearly indepen-
dent of ℓ, r, and the pair of ℓ_{cutoff}'s, we conclude that our choices
of the functional forms of the eddy viscosities and diffusivity
are self-consistent for $R_s = 10^{10}$. It is also reassuring that the three
eddy coefficients are nearly the same and are all of order unity. For
the remainder of the numerical results presented in this paper,
we have held C_p, C_T and C_K fixed at their averaged values of 0.46,
0.55, and 0.52 respectively.

III. TIME-AVERAGED NUMERICAL RESULTS

A) Temperature and Flux

We have computed a numerical solution for convection in a sphere with a Rayleigh number, R_s, of 10^{10}, and a Prandtl number, P_r, of 1, and with the boundary conditions and dimensionless units described in Paper II. The heat source, $H(r)$, is constant for $r<0.3$ and zero outside of this radius. We have used the time-averaged eddy coefficients described in §2. Although the convective solution is time-dependent, the energy spectra are time-independent when averaged over several of the largest eddy turn-over times; the results presented in this section have been averaged over ~ 30 eddy turnover times. We use the notation that single brackets, $< >$, around a quantity indicate an average over θ, ϕ and double brackets, $<< >>$, indicate an average over θ, ϕ, and t. The horizontal and time-averaged temperature as a function of radius, $<<T(r)>>$, is shown in Figure 1. The fluid is nearly isothermal except at the outer boundary which has a thickness of ~ 0.03. By an asymptotic expansion it can be shown that $\left|\frac{\partial T}{\partial r}\right| \sim (R_s)^{-1/3} \simeq 5\times10^{-4}$ far away from the boundary layer. The time-averaged numerical results are not inconsistent with this value, but at any particular value of radius and time the fluctuation in $\left|\frac{\partial T}{\partial r}\right|$ can be 10-100 times this value (see §3). The central temperature is $<<T(0)>>=0.036$, which should be compared to the central temperature of 0.68 calculated with $R_s = 10^4$, $P_r = 10$ (Paper II) and a central temperature of 4.0 for a fluid in conductive equilibrium. Although $\left|\frac{\partial T}{\partial r}\right|$ scales as $(R_s)^{-1/3}$, the central temperature scales as $\left|\frac{\partial T}{\partial r}\right| \times$ boundary-layer thickness. Since the turbulent boundary-layer thickness

has a slight Rayleigh number dependence, $<<T(0)>>$ scales only
approximately as $(R_s)^{-1/3}$. Figure 1 shows a slight bump at $r=0.3$
which is the boundary of the heat source. This bump is not nearly
as prominent as it was for $R_s=10^4$, and we conclude that at large
Rayleigh numbers, the convective velocity is very efficient in
smoothing out the temperature perturbations due to the inhomogeneities in the
heat source. The mean temperature curve also shows that the
temperature gradient, $<< \frac{\partial T}{\partial r} >>$, is positive near the origin and
near the outer boundary layer. In these two regions, the conduc-
tive flux transports energy toward the center of the star; the
time-averaged convective flux due to all modes, Total F_{con}, is
greater than the steady-state flux of the heat source,
$F_{ss}(r)=(4\pi r^2)^{-1} \int_0^r H(r')dr'$. We have plotted the ratio of these two
fluxes in Figure 2. Far away from the boundary-layer this ratio
should be $\sim 1-(R_s)^{-1/3}$. Convective overshoot is indicated where
Total F_{con}/F_{ss} is greater than 1. Because Total $F_{con} \approx F_{ss}$ and is
so much greater than the conductive flux, there can be large (10-
100) fluctuations in the conductive flux (i.e. temperature grad-
ient) without affecting the total flux. Plotted on the curve in
Figure 2 with error bars is the variance of Total F_{con}/F_{ss} (The
variance σ of a quantity x is with respect to time,
$\sigma \equiv [<<(x-<<x>>)^2>>]^{1/2}$). The variance of the total (convective +
conductive) flux divided by F_{ss} is nearly identical to the variance
shown in Figure 2. The increase in σ with radius is due to the
fact that the local Rayleigh number in the surface boundary-
layer is near its critical value. Secondary convective insta-

bilities in the boundary-layer cause time-dependent bursts in the convective flux. These fluctuations propagate inward and diminish in amplitude as they approach the origin. Notice that the variance at the surface is $\sim$ 18% of the total flux.

B) 2- and 3-Dimensional Spectra

The time-averaged kinetic and fluctuating thermal energy spectra (see Paper II for definitions) at r=0.5 as functions of the 2-dimensional wavenumber, ℓ, are shown in Figure 3. Both spectra behave as power laws at large ℓ, but for $\ell \leq 6$ the kinetic energy spectrum is nearly exponential and obviously shows the effects of production. The thermal energy spectrum has a noticeable "cliff" between $\ell=4$ and $\ell=5$. Each spectrum is normalized by the total energy at r=0.5 (due to all modes).

In dimensionless units the kinetic energy (which scales as $R_s^{2/3}$) at r=0.5 is $\sum_\ell KE(\ell,r=0.5)=6.26\times10^7$. Approximately 91% of this energy is in the $\ell=1$ modes. The fluctuation thermal energy (which scales as $R_s^{-2/3}$) at r=0.5 is 4.52×10^{-6} and approximately 35% of this energy is in the $\ell \sim 1$ modes. The variances of the $\ell = 1$ component of the kinetic and thermal energies are .08 KE(1, 0.5) and 0.2 TE(1, 0.5), respectively. The energies of the three $\ell = 1$ modes ($Y^{R,1,0}$, $Y^{R,1,1}$ and $Y^{I,1,1}$) completely change in one eddy turnover time. If the three modes were statistically independent, then the $\ell = 1$ kinetic and thermal energy would each have a fractional variance of $1/\sqrt{3}$. Because our numerically determined variances are much smaller, the three $\ell = 1$ components of the kinetic and thermal energies must be very well correlated with each other. The 2-dimensional kinetic energy spectrum has been deconvolved into a 3-dimensional spectrum and plotted as a function of the log of the 3-dimensional wavenumber, k, in Figure 4. The dashed line is $k^{-5/3}$ and is provided for comparison with a Kolmogorov

spectrum. The spectrum clearly shows a production peak at the low wavenumbers, a cliff at $k \approx 3$ and an equilibrium range for $k>6$. The wavenumber of the Kolmogorov length calculated from rate of kinetic energy dissipation (§3.d) is $\sim 3 \times 10^3$. As discussed in Paper II, approximations are introduced into the transformation of a 2-dimensional spectrum into a 3-dimensional spectrum, so the 5/3-power-law behavior of Figure 4 should be viewed with some caution.

The kinetic energy $KE(\ell,r)$ as a function of radius is graphed for each value of ℓ in Figure 5. The curves are qualitatively the same as they were for $R_s=10^4$, $P_r=10$ (Paper II). Except for $\ell=1$ and $\ell=12$ each curve is zero at the origin, rises to a peak at $0.5<r<0.8$, decreases to a local minimum, and then increase sharply in the outer boundary-layer. The peak shifts to larger values of radius with increasing ℓ. Using the distance between the local minimum of $KE(\ell,r)$ and $r=1.0$ as the turbulent boundary-layer thickness, we see that the thickness is fairly constant for $\ell>6$. The turbulent boundary-layer is due to our eddy viscosity. The viscous sublayer, with a thickness of $\sim KE(\ell,r=1)^{-1/2}$, is unresolvable. For $\ell=12$, the local minimum in $KE(\ell, r)$ denotes that the turbulent boundary-layer has disappeared. The disappearance is because our eddy viscosity dominates the $\ell=12$ mode not just in the boundary-layer but for all values of r.

The time-averaged fraction of the total convective flux at $r=0.5$ that is carried by modes of wavenumber ℓ, $F_{con}(\ell)/\text{Total } F_{con}$, is plotted in Figure 6. Far from being a smooth power law spectrum, we see that: (1) over 90% of the convective flux is carried by the $\ell=1$ modes, (2) virtually no flux is carried by modes with $\ell \gtrsim 6$, and (3) the $\ell=3$ modes advect energy <u>downward</u>. The convective flux carried by the modes of wavenumber ℓ, is

$$\sum_{\gamma,m} <(e_r \cdot \underline{v})_{\gamma,\ell,m} \, T_{\gamma,\ell,m}> \, .$$ We therefore expect $F_{con}(\ell)/\text{Total } F_{con}$ to be proportional to the square root

of the product of the kinetic and thermal energy spectra. We also expect $F_{con}(\ell)$ to be proportional to the correlation between the radial velocity and temperature:

$$\delta(\ell,r) \equiv \sum_{\gamma,m} (e_r \cdot \underline{v})_{\gamma,\ell,m} T_{\gamma,\ell,m} / \{ \sum_{\gamma,m} [\hat{e}_r \cdot \underline{v})_{\gamma,\ell,m}]^2 \quad\quad (3.1)$$
$$\times \sum_{\gamma,m} [T_{\gamma,\ell,m}]^2 \}^{1/2}$$

We have found that there is a slow, systematic decrease in $\delta(\ell,r)$ with increasing ℓ. The decrease means that the large scale velocity and temperature have better spatial correlation than the small scale velocity and temperature. The time-averaged correlation, $<<\delta(\ell,r)>>$, decreases more rapidly with ℓ then does $<\delta(\ell,r)>$, indicating that the large scale velocity and temperature modes are also better correlated in time than are the small scale modes. Note that $<<\delta(\ell=3, r=0.5>>$ is less than zero because the $\ell=3$ convective flux is negative. The time-averaged total correlation of the radial velocity and temperature for all ℓ is

$$<<\delta(r)>> \equiv <<[<v_r \tilde{T}>/(<v_r^2><\tilde{T}^2>)^{1/2}]>> \quad\quad (3.2)$$

In Figure 7 we have plotted $<<\delta(r)>>$ as a function of radius. The correlation varies between 0.5 and 1.0. In comparison, Deardorff and Willis (1967) find that in plane-parallel convection in air ($P_r \approx .7$) with a Rayleigh number of 10^7, the correlation $\delta(r)$ varies between 0.5 and 0.7. They also find a decrease in the correlation, δ, with wavelength.

C) Isotropy

As in Paper II, we have used $I(\ell,r) \equiv KE_H(\ell,r)/2KE_R(\ell,r)$ as a
measure of the isotropy at the flow where $KE_R(\ell,r)$ is the kinetic
energy in the radial direction at r due to motions of wavenumber ℓ,
and where $KE_H(\ell,r)$ is the kinetic energy in the horizontal direction.
When $I(\ell,r) \approx 1$, the flow is isotropic. In Paper II, it was shown
that for all ℓ, $I(\ell,r)$ is constrained to be equal to 1 at r=0.
Furthermore, in the outer boundary layer, the radial component of
the velocity goes to zero, so $I(\ell,r)$ goes to infinity.
The ratio, $KE_H(\ell,r)/2KE_R(\ell,r)$, is a useful measure of isotropy only
for $0.2 \leq r \leq 0.8$. The isotropy is plotted as a function of r for all
ℓ in Figure 8. The $\ell=1$ isotropy is qualitatively similar to the
values calculated with $R_s = 10^4$, $P_r = 10$ (Paper II); the radial component
of the velocity dominates except in the boundary-layer. For $R_s=10^4$
we found that the radial velocity was dominant for all ℓ. Figure
8 shows that for $\ell \geq 3$ the horizontal component of the velocity
becomes important at some values of the radius. More importantly,
for large values of ℓ, $[I(\ell,r)-1]$ becomes small for r<0.8,
indicating that the flow becomes isotropic at large wavenumbers.
Note that $I(\ell,r)$ for $\ell=12$ increases monotonically from r=.2 to
r=.8; this behavior is due to the eddy viscosity.

D) Energy Budgets

We find that the time-averaged rate at which fluctuating
thermal energy enters the fluid due to all modes, TE_{in}, is 0.166
and the time-averaged rate at which kinetic energy enters the

fluid due to all modes, KE_{in}, is 6.01×10^{10}. In Paper II we showed that KE_{in} for an isothermal fluid is $1.892\pi\times P_r R_s \approx 5.9\times10^{10}$; we see that the calculated and isothermal values of KE_{in} are nearly the same. In Figure 9 we have plotted $KE_{in}(\ell)$ and $TE_{in}(\ell)$, the rates at which kinetic and fluctuating thermal energy obtained directly from buoyancy (not from cascading) enter the shell of modes with wavenumber ℓ. The definitions $TE_{in}(\ell)$ and $KE_{in}(\ell)$ in terms of modes appear in Paper II. Figure 9 shows that $\sim 87\%$ of KE_{in} and $\sim 74\%$ of TE_{in} are due to the $\ell=1$ modes. Note that $KE_{in}(\ell=3)$ is negative, which means that the $\ell=3$ velocity and temperature fluctuations are <u>negatively</u> correlated [i.e. $\delta(\ell=3,r)<0$]. For $\ell>3$, $KE_{in}(\ell)/KE_{in}$ and $TE_{in}(\ell)/TE_{in}$ are both much less than 1 so the production part of the spectrum is confined to $\ell\lesssim3$.

The rate at which fluctuating energy cascades into the set of modes with wavenumber ℓ is

$$TE_{cas}(\ell) = -4\pi \sum_{\gamma,m} \int_0^1 <(\underline{v}\cdot\nabla T)_{\gamma,\ell,m}\ T_{\gamma,\ell,m}>r^2dr.$$

We can arbitrarily write this rate as the difference

$$TE_{cas}(\ell) = TE_{up}(\ell) - TE_{down}(\ell) \tag{3.3}$$

where

$$TE_{up}(\ell) = -4\pi\sum_{\gamma,m}\int_0^1 <(\underline{v}\cdot\nabla T_<)_{\gamma,\ell,m}\ T_{\gamma,\ell,m}>r^2dr \tag{3.4}$$

$$TE_{down}(\ell) = 4\pi\sum_{\gamma,m}\int_0^1 <(\underline{v}\cdot\nabla T_>)_{\gamma,\ell,m}\ T_{\gamma,\ell,m}>r^2dr \tag{3.5}$$

and where

$$T_> = \sum_{\ell' > \ell} T_{\ell'} \tag{3.6}$$

and

$$T_< = \sum_{\ell' < \ell} T_{\ell'} \tag{3.7}$$

Physically, we can think of $TE_{up}(\ell)$ as the rate at which the thermal energy cascades into the modes with wavenumber ℓ due to thermal fluctuations larger than the wavelength of the ℓ-modes, and $TE_{down}(\ell)$ as the rate at which the thermal energy of the modes of wavenumber ℓ feeds the smaller thermal fluctuations. If there were no dissipation, then:

$$TE_{in}(\ell) + TE_{up}(\ell) = TE_{down}(\ell) \tag{3.8}$$

We plot $TE_{up}(\ell)/TE_{down}(\ell)$ in Figure 10 and use this ratio to determine whether or not the wavenumber ℓ belongs in the production or inertial range. For $\ell=0$, $TE_{up}(\ell)$ must equal zero. As ℓ increases the ratio goes smoothly to 1. For $\ell \geq 6$, $TE_{up}(\ell)/TE_{down}(\ell) \approx 1$, which indicates that $TE_{in}(\ell) << TE_{up}(\ell)$ or equivalently that the modes with wavenumber ℓ derive most of their energy from the cascade and not from direct production; ℓ lies in the inertial range for $\ell \geq 6$. We can define $KE_{up}(\ell)$ and $KE_{down}(\ell)$ in a fashion similar to equations (3.4) and (3.5). The ratio $KE_{up}(\ell)/KE_{down}(\ell)$ shown in Figure 10 is near unity for $\ell > 6$, indicating that the kinetic energy spectrum is also inertial for $\ell \geq 6$. For $\ell=3$ the ratio of $KE_{up}(\ell)$ to $KE_{down}(\ell)$ is anomalously large because $KE_{in}(\ell=3)$ is negative (see Figure 9).

Because we are numerically limited to a finite resolution, we can only approximate nonlinear quantities such as $TE_{up}(\ell)$ and $TE_{down}(\ell)$. The approximation used in evaluating $TE_{up}(\ell)$ is

$$<T_{\gamma,\ell,m}(\underline{v}\cdot\nabla T_<)_{\gamma,\ell,m}> \simeq <T_{\gamma,\ell,m}(\hat{\underline{v}}\cdot\nabla T_<)_{\gamma,\ell,m}> \qquad (3.9)$$

where $\hat{\underline{v}}$ is the numerically resolvable part of $\underline{v}$ (see §2). Using the eddy diffusivity, $\mathcal{R}_e^{\gamma,\ell,m}$, that was introduced in §2, we compute $TE_{down}(\ell)$ with the approximation

$$\int_0^1 r^2 dr \ <T_{\gamma,\ell,m}(\underline{v}\cdot\nabla T_>)_{\gamma,\ell,m}> \simeq$$

$$\int_0^1 r^2 dr \ \{<T_{\gamma,\ell,m}(\hat{\underline{v}}\cdot\nabla\hat{T}_>)_{\gamma,\ell,m}>$$

$$- <T_{\gamma,\ell,m}\nabla\cdot[\mathcal{R}_e^{\gamma,\ell,m}\nabla(T_{\gamma,\ell,m} \ Y^{\gamma,\ell,m})]>\} \qquad (3.10)$$

where $\hat{T}_>$ is the resolvable part of $T_>$. The approximation in (3.11) is based on both the definition of $\mathcal{R}_e^{\gamma,\ell,m}$ and the assumption that the energy cascade is local in wavenumber space. We see from (3.11) that two terms contribute to $TE_{down}(\ell)$: one due to the resolvable part of the temperature and the other to the unresolvable part that is parameterized by the eddy diffusivity.

In Figure 11 we plot the fraction of $TE_{down}(\ell)$ that is due to the eddy diffusivity, $TE_{down}^{eddy}(\ell)/TE_{down}(\ell)$, as a function of ℓ. Figure 11 shows that the eddy diffusivity has a negligible contribution to $TE_{down}(\ell)$ for $\ell<9$. This means that the eddy diffusivity has little effect on the large scale modes; it directly affects only the small scale modes. The large scale modes feel the eddy diffusivity only through the nonlinear interactions with the small scale modes. In Figure 11 we have also plotted the ratio,

$KE_{down}^{eddy}(\ell)/KE_{down}(\ell)$ that is the fraction of $KE_{down}(\ell)$ due to

the unresolvable part of $\underline{v}$ parameterized through the eddy vis-

cosities. Again, it is only the small scale modes that directly

feel the eddy viscosities.

IV. TIME-DEPENDENT RESULTS

A) Instantaneous Velocity and Temperature

The velocity and temperature are time-dependent and are

self-correlated for approximately one eddy

turn-over time. We estimate the turnover time of the largest

eddies as $2\times<<\underset{\sim}{\underline{v}}^2(r=0)>>^{-1/2}\approx 3\times 10^{-4}$. When averaged over many turn-

over times, $\underline{v}$ and T are zero. The $Y^{R,1,0}$ components of the temp-

erature, poloidal, and toroidal velocities at one particular instant

in time are plotted in Figures 12, 13 and 14 respectively. The

plotted functional forms of the $\ell=1$ temperature and poloidal velo-

city are characteristic of the forms for all values in time; it

is only the amplitude of the functional form of the largest $\ell=1$

mode that changes rapidly in time as the three $\ell=1$ modes take turns

dominating the temperature and poloidal velocity. These functional

forms are similar to those found in Paper II

for $R_s=10^4$, $P_r=10$. The poloidal velocity smoothly decreases from

its maximum value at the origin to zero at the surface, with no

nodes and with no trace of the $r=0.3$ shell that marks the bound-

ary of the internal heat source. In contrast, the functional form

of the high ℓ components of the poloidal velocity does change in

time. The number of nodes in the poloidal velocity (which corre-

sponds physically to the number of radially stacked convective

eddies) increases with ℓ and is ~ 4 for $\ell=12$. The functional

form of the $\ell=1$ temperature shown in Figure 12 is doubly peaked
with a small peak near the boundary-layer and a large peak at
$r=0.3$. The toroidal component of the velocity is plotted as
$r^3\psi^{R,1,0}$ in Figure 14 and is the angular momentum about the
z-axis. Conservation of angular momentum requires that
$\int_0^1 r^3\psi^{R,1,0}dr=0$ for all time. The functional form of $r^3\psi^{R,1,0}$
changes dramatically in one eddy turnover time. No rotation law
can be ascribed to the flow because for all values of radius the
time-averaged value of $r^3\psi^{R,1,0}$ is zero. It is important to realize
that this numerical result, does not immediately follow from angular
momentum conservation.

B) Intermittency

We have calculated some of the standard measures of inter-
mittency, such as the departure of the inertial spectrum from $k^{-5/3}$
and the kurtosis of the high-order structure functions. However,
due to our limited spatial resolution, our numerically computed
values are not quantitatively useful measures of the spatial
intermittency. Siggia and Patterson (1979), working in a finely resolved
Cartesian geometry have calculated the spatial intermittency for
an isothermal fluid that is driven not by buoyancy but by a
large-scale, isotropic, permanently frozen-in velocity field.
Instead of trying to reproduce their results in a sphere of con-
vecting fluid, we present some quantitative measures of the time-
dependence of the intermittency. Figure 15 shows the variations
in the convective flux, $[F_{con}-<<F_{con}>>]/<<F_{con}>>$ at $r=0.5$ as a
function of time. The dashed line corresponds to the variance,

σ, (calculated over 30 eddy turnover times) in units of $<<F_{con}>>$.
Each timestep plotted in Figure 15 is 3×10^{-7} units of dimension-
less time. Each 1000 timesteps is roughly one eddy turnover time.
There is a burst in the convective flux near iteration number
2500. The fluctuation is of order 2σ and lasts for approximately
one half of an eddy turnover time. We have found 4 bursts similar
to the one illustrated in Figure 15 while examining the convective
flux for 30 eddy turnover times. The bursts in flux are asso-
ciated with bursts in the kinetic and thermal energy spectra.
The fluctuations in these spectra at $r = 0.5$
for odd values of ℓ are shown in Figures 16 and 17 as a function of
time. The dashed lines correspond to the variances of the energy.
All bursts are of order 2σ and clearly cascade from the
low to the high wavenumber modes. It takes roughly one half of an
eddy turnover time for the kinetic energy bursts to cascade from
$\ell=1$ to $\ell=9$. The thermal energy cascade is slower and it requires
nearly one turnover time to cascade from $\ell=1$ to $\ell=9$. Each of the
bursts is initially positive, then followed by damped oscillations.
We have never observed a burst that is initially negative.

The fluctuations seem to arise from a secondary convective
instability in the boundary-layer where the local Rayleigh num-
ber is never far from its critical value. The fluctuations prop-
agate inward from the surface via the $\ell=1$ modes, then cascade
downward in wavelength. The fluctuations in the high wavenumber
modes at $r=.5$ are not caused by high wavenumber fluctuations that
travel directly from the boundary-layer to $r=.5$, but are due to
energy cascading from low to high wavenumbers at $r=.5$. To prove
this, we have shown that for $\ell>2$, the 2σ fluctuation in $TE(\ell,r=.5)$

occurs just after a strong fluctuation in $\sum_{\gamma,m} (\underline{v}\cdot\nabla T_<)_{\gamma,\ell,m} T_{\gamma,\ell,m}$ at $r=.5$.
The latter fluctuation is indicative of a cascade from big to small

modes. Furthermore, we repeated the calculation starting with

iteration #1300 as the initial data. In the repeated calculation

we artificially set the $(\underline{v}\cdot\nabla T_<)_{\gamma,\ell,m}$ contribution to $(\underline{v}\cdot\nabla T)_{\gamma,\ell,m}$

equal to zero. We then found that there was still a 2σ fluctuation

in the $\ell=1$ modes, but that the fluctuations in $KE(\ell,r=.5)$

for $\ell>2$ were less than one σ. This proves that the

$\ell>2$ fluctuations are caused by energy cascading from big to

small modes via the $(\underline{v}\cdot\nabla T_<)$ terms.

V. CONCLUSIONS

We have been able to show that for sufficiently high Ray-

leigh numbers, a convecting fluid develops an inertial subrange

(in which the flow is nearly isotropic and the energy spectrum

$\simeq k^{-5/3}$) and that part of this subrange can be resolved numeri-

cally. The anisotropy of the flow and fine structure of the

energy spectra are confined to the largest wavelengths. The

effects of the unresolvable part of the inertial subrange can

be modeled with an eddy viscosity and diffusivity that are func-

tions only of the local values of the velocity field. The ampli-

tudes of the eddy viscosities and diffusivity can be determined

by requiring that the computed solutions be independent of the

limit of spatial resolution. This method of computing the eddy

viscosity fails to work if the limit of spatial resolution does

not lie in the inertial subrange. Because we need a well-defined

inertial range, our method of computing eddy viscosities requires

that the Reynolds and Peclet numbers are large. We have
found that the poloidal and toroidal parts of the eddy viscosity
are nearly equal and that the eddy diffusivity is $\sim$ 10% greater
than the poloidal part of the eddy viscosity.

The important results obtained with these eddy viscosities
with a Rayleigh number of 10^{10} and a Prandtl number of unity can
be summarized as follows:

1) The fluid motions are time-dependent and have no spatial
   symmetries.

2) An examination of the kinetic and fluctuating thermal
   energy spectra as a function of wavelength as well as
   a study of the manner in which energy cascades in and
   out of each wavelength shows that there is an inertial
   range for $\ell \gtrsim 7$.

3) A computation of the ratio of the horizontal to the
   radial component of the kinetic energy shows that flow
   tends toward isotropy at $\ell \gtrsim 7$.

4) Except at the outer boundary-layer, nearly all of the heat
   flux is carried by convection. There is overshooting at
   the center and near the boundary-layer, causing the con-
   ductive flux to transport energy toward the center of the
   sphere.

5) The variance, σ, (with respect to time) of the flux
   increases from the center to the surface of the sphere.
   At the surface, σ is $\sim$ 18% of the total flux. The increase
   in σ near the surface is probably due to a secondary con-
   vective instability in the boundary-layer.

6) The boundary-layer instabilities result in a series of
   intermittent bursts in flux and energy at all radii.
   The bursts in the energy cascade from the large, $\ell=1$, to
   the small, $\ell=9$, wavelengths requires approximately one
   half of an eddy turnover time for the kinetic energy and
   about one eddy turnover time for the thermal energy.

ACKNOWLEDGMENTS

REFERENCES

Deardorff, J.W. 1972, J. Atmos. Sci., 29, 91.

Deardorff, J. W., and Willis, G. E. 1967, J. Fluid Mech., 28, 675.

Kraichnan, R. H. 1976, J. Atmos. Sci., 33, 1521.

Ledoux, P., Schwarzschild, M., and Spiegel, E. A. 1961, Ap. J.,
    133, 184.

Marcus, P. M. 1980a, submitted to Ap. J (Paper II).

Marcus, P. M. 1980b, submitted to Journal of Fluid Mech.

Schlesinger, R. E. 1978, J. Atmos, Sci., 35, 2268.

Siggia, E. D., and Patterson, G. S. 1978, J. Fluid Mech., 86, 567.

Tennekes, H., and Lumley, J. L. 1972, A First Course in Turbulence,
    (Cambridge, Massachusetts: MIT Press).

FIGURE CAPTIONS

Figure 1 - The time-averaged mean temperature as a function of
radius. The break in the curve at r=0.3 marks the bound-
ary of the internal heat source.

Figure 2 - The ratio of the time-averaged convective flux carried
by all of the modes to the steady-state flux due to the inter-
nal heat source as a function of radius. Overshooting occurs
near the origin and boundary-layer. The variances of the
ratio of fluxes is plotted with error bars and reaches a
maximum near the boundary-layer.

Figure 3 - The time-averaged 2-dimensional spectra of kinetic
and fluctuating thermal energy as a function of ℓ at r=0.5.
For $\ell \gtrsim 7$, the spectra behave as power laws.

Figure 4 - The time-averaged kinetic energy spectrum as a func-
tion of the 3-dimensional wavenumber, k. The dashed line
has a slope of -5/3 and corresponds to a Kolmogorov spec-
trum.

Figure 5 - The time-averaged kinetic energy spectra $KE(\ell,r)/r^2$
as functions of radius for $\ell=1,12$. The spectra are similar
to the results obtained with $R_s=10^4$, $P_r=10$ in that the radius
at which the peak of each spectrum occurs increases with ℓ.
Each spectrum is normalized by its maximum value, KE_{max}/r^2.

Figure 6 - The ratio of the convective flux carried by modes of
wavenumber ℓ to the total convective flux carried by all
modes. The figure is computed at r=0.5. The negative value

of the ratio at $\ell=3$ indicates that the $\ell=3$ modes are per-
forming mechanical work on the fluid.

Figure 7 - The time-averaged correlation of the radial velocity
and temperature $<<\delta>> \equiv << <v_r T>/<v_r^2>^{1/2}<T^2>^{1/2}>>$. The
variance of the correlation is denoted by error bars.

Figure 8 - The ratio of the horizontal kinetic energy to twice
the radial kinetic energy as a function of radius for each
wavenumber ℓ. By definition, the ratio is 1 at the origin
and goes to infinity in the boundary-layer where the radial
component of the velocity vanishes. The ratio is a good
measure of the isotropy for $0.2 \leq r \leq 0.8$. As ℓ increases, the
ratio goes to unity, demonstrating that the flow becomes
nearly isotropic at small wavelengths.

Figure 9 - The fraction of the total amount of kinetic (thermal)
energy generated that is produced by modes of wavenumber ℓ
is shown by solid (open) circles. Negligible energy pro-
duction occurs when $\ell \gtrsim 6$.

Figure 10 - The ratio of the rate at which kinetic (thermal)
energy cascades into modes of wavenumber ℓ from all larger
wavelength modes to the rate at which kinetic (thermal) energy
cascades from the modes of wavenumber ℓ to all smaller wave-
length modes. By definition the ratio must be zero for $\ell=1$.
For $\ell>6$ the ratio approaches unity and is indicative of an
inertial range where production and dissipation are unimportant.

Figure 11 - The rate at which kinetic (thermal) energy cascades
from modes of wavenumber ℓ to wavelengths smaller than the
limit of numerical resolution to the rate at which the energy
cascades from ℓ to all smaller wavelength modes. The rate
at which the energy cascades to the modes smaller than the
resolution limit is computed with the eddy viscosity (diffu-
sivity). The plotted ratio shows that only modes with $\ell > 9$
directly feel the eddy viscosity (diffusivity).

Figure 12 - The instantaneous temperature of the $Y^{R,1,0}$ mode
as a function of radius. The functional form of this mode
with one peak at $r=0.3$ and the other at the boundary-layer
is typical of the largest $\ell=1$ mode.

Figure 13 - The same as Figure 12, except the radial
component of the velocity, $\ell(\ell+1)\ \omega_{R,1,0}/r$, is shown
here.

Figure 14 - The same as Figure 13, except with the toroidal com-
ponent of the velocity. The angular momentum about the
z-axis is $4\pi r^3 \psi_{R,1,0}$, so $\int_0^1 r^3 \psi_{R,1,0} = 0$. The
functional form of $r^3 \psi_{R,1,0}$ changes in an eddy turnover
time.

Figure 15 - The deviations of the convective flux from its time-
averaged value $<<F_{con}>>$ as a function of time. The figure is
computed at $r=0.5$. The dashed lines are the variance, σ,
of F_{con} in units of $<<F_{con}>>$. One eddy-turnover time is
approximately equal to 1000 timesteps.

Figure 16 -The same as Figure 15 for kinetic energy. The burst in energy requires $\sim$ half a turnover time to cascade from $\ell=1$ to $\ell=9$.

Figure 17 - The same as Figure 17 for the fluctuating thermal energy. The thermal energy cascade is slower than the kinetic energy cascade and requires nearly one full turn-over time to cascade from $\ell=1$ to $\ell=9$.
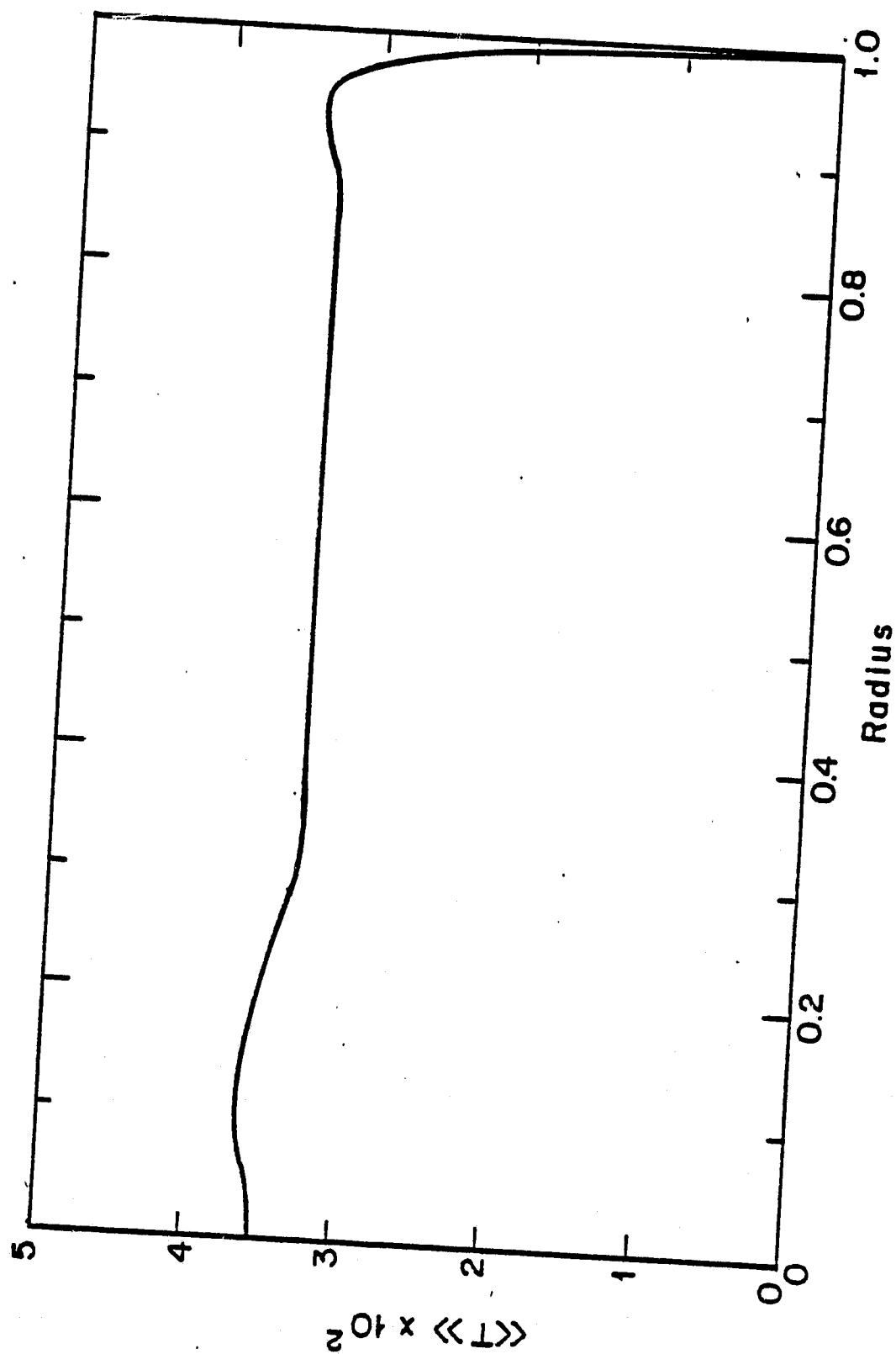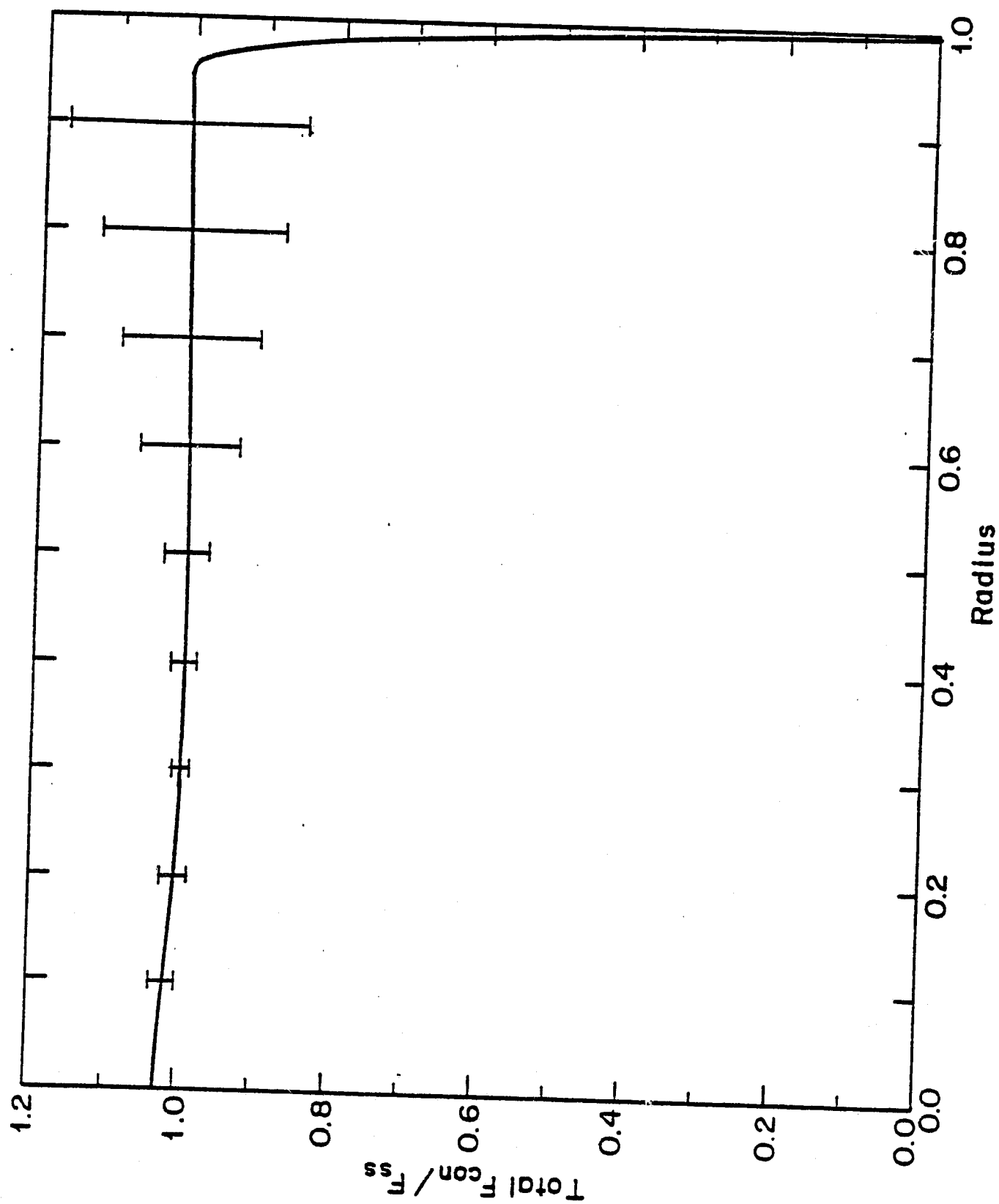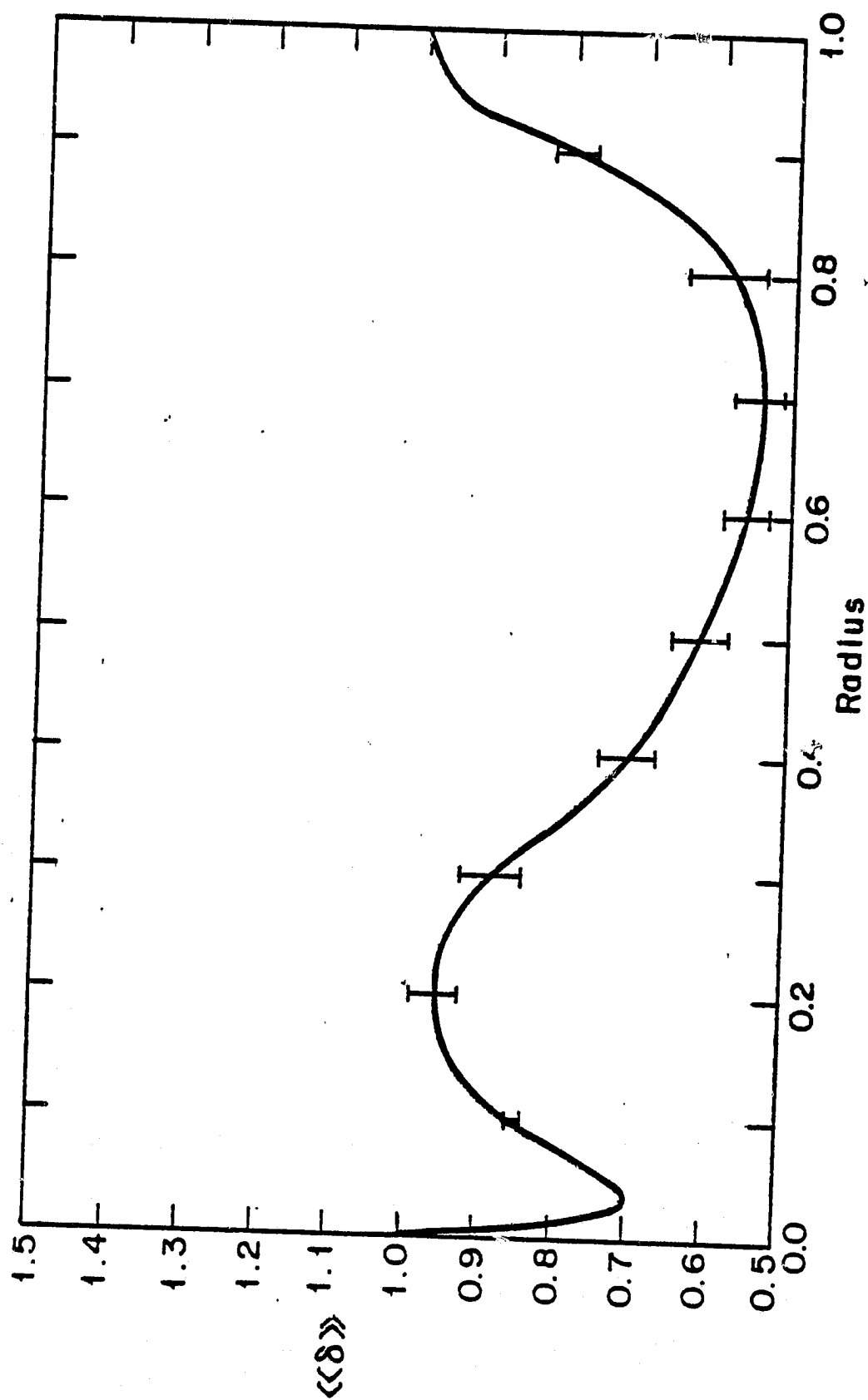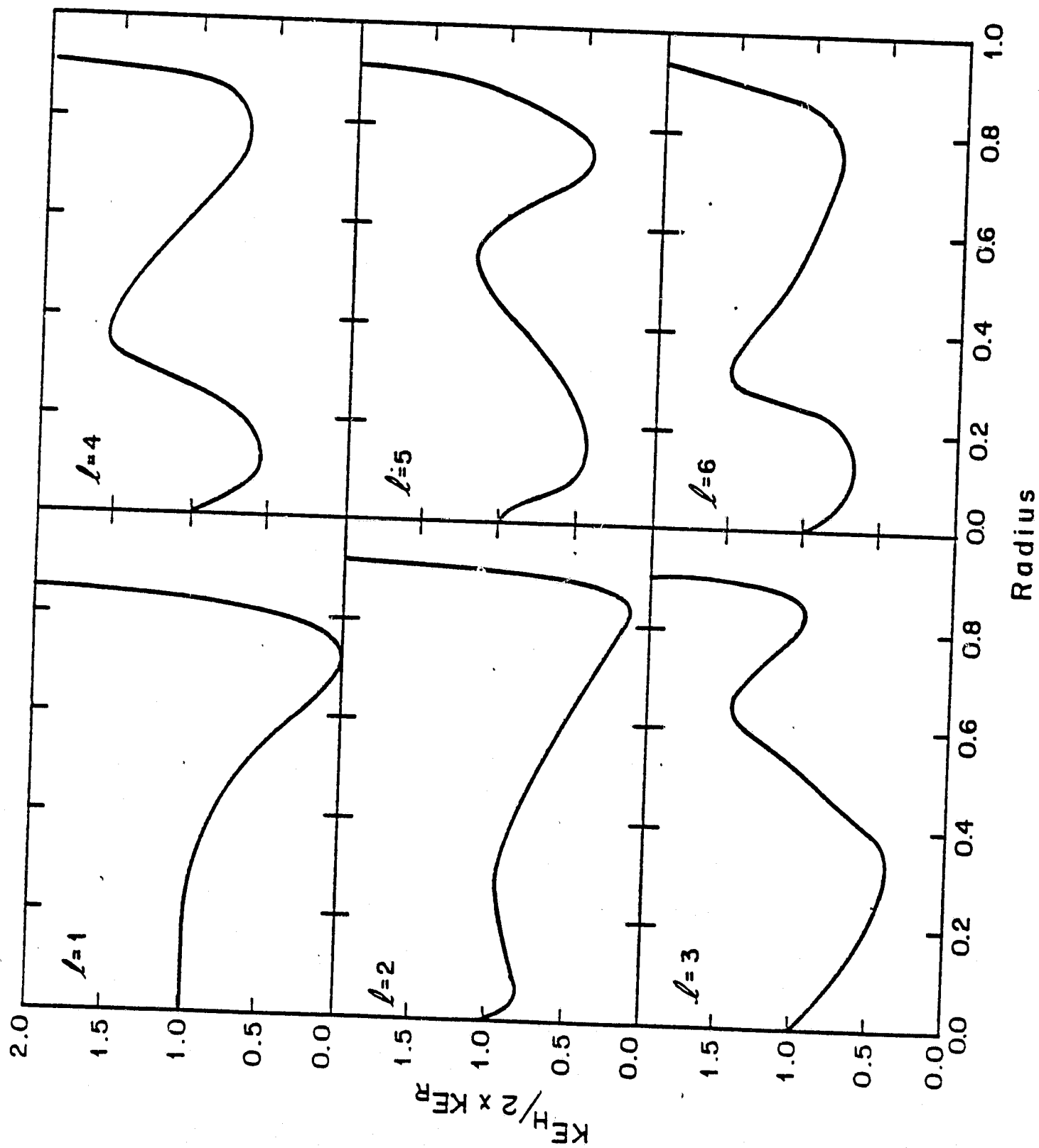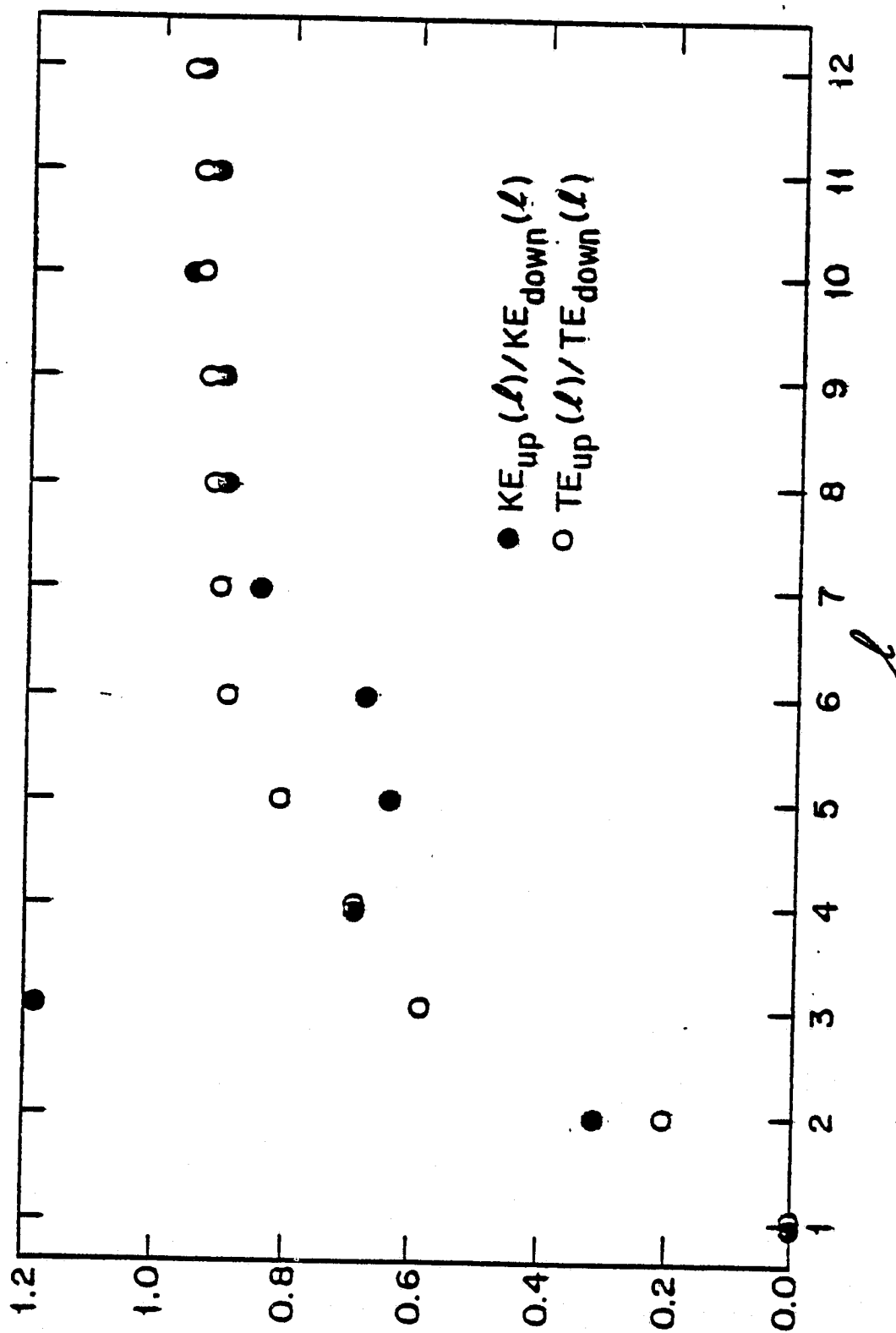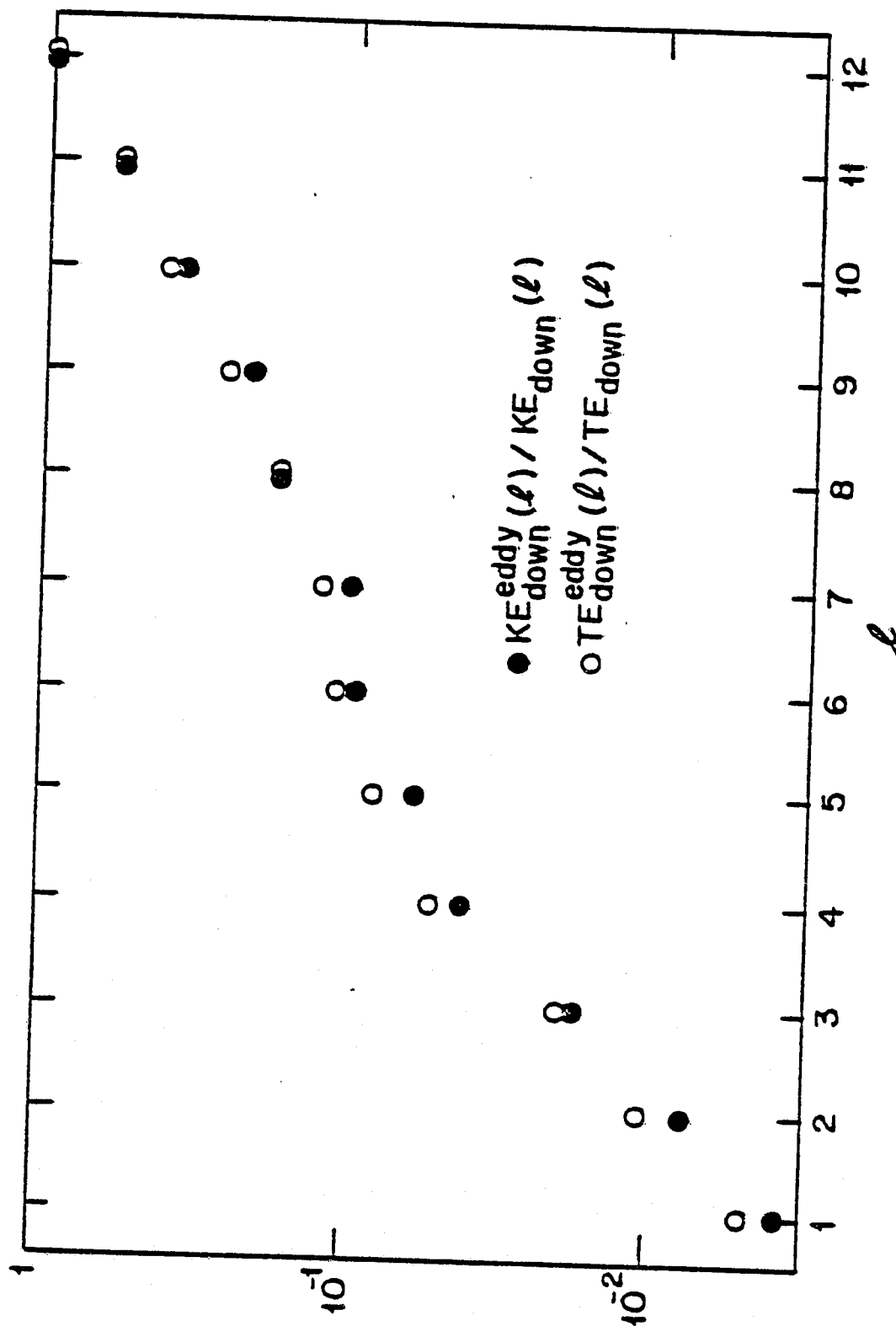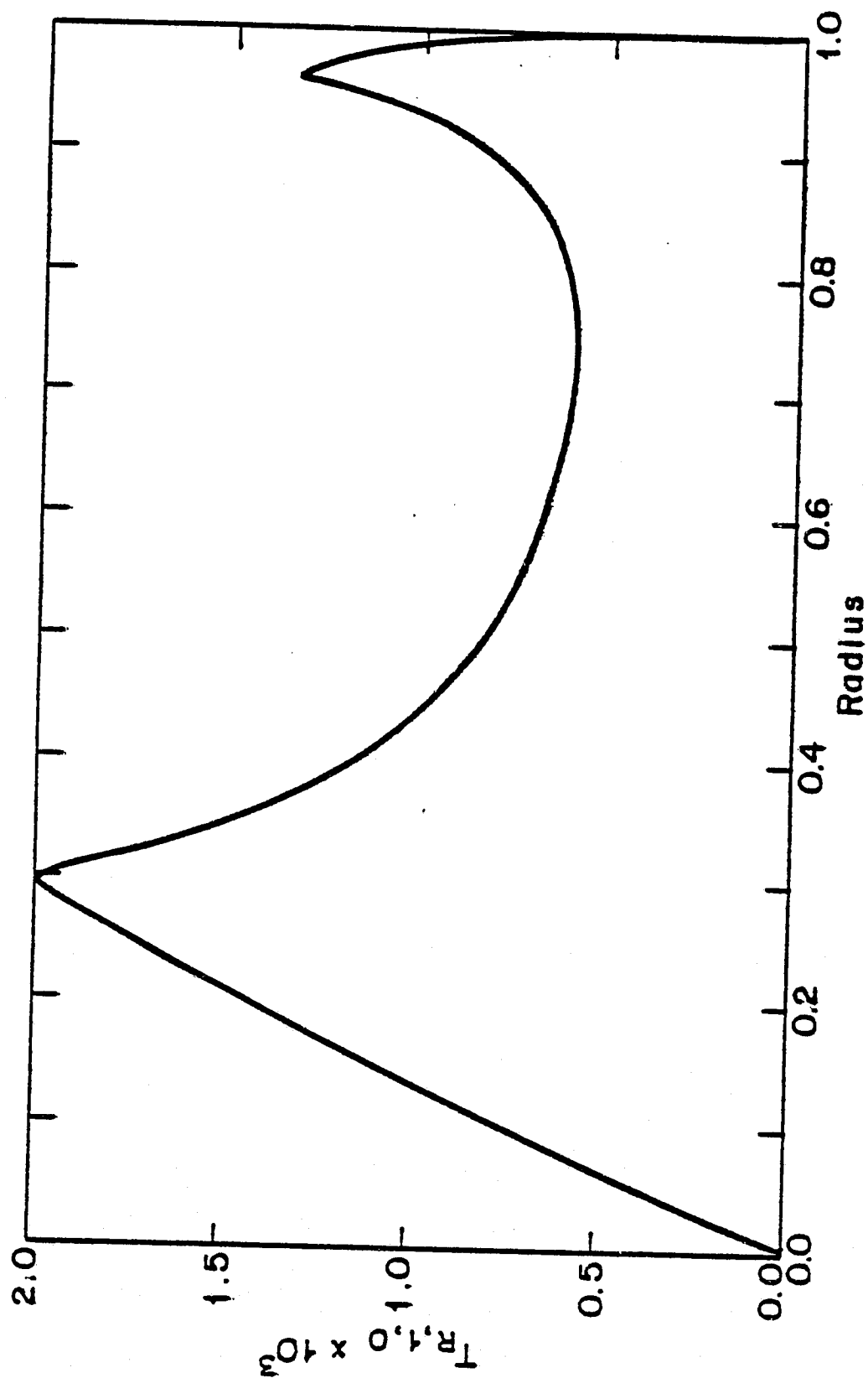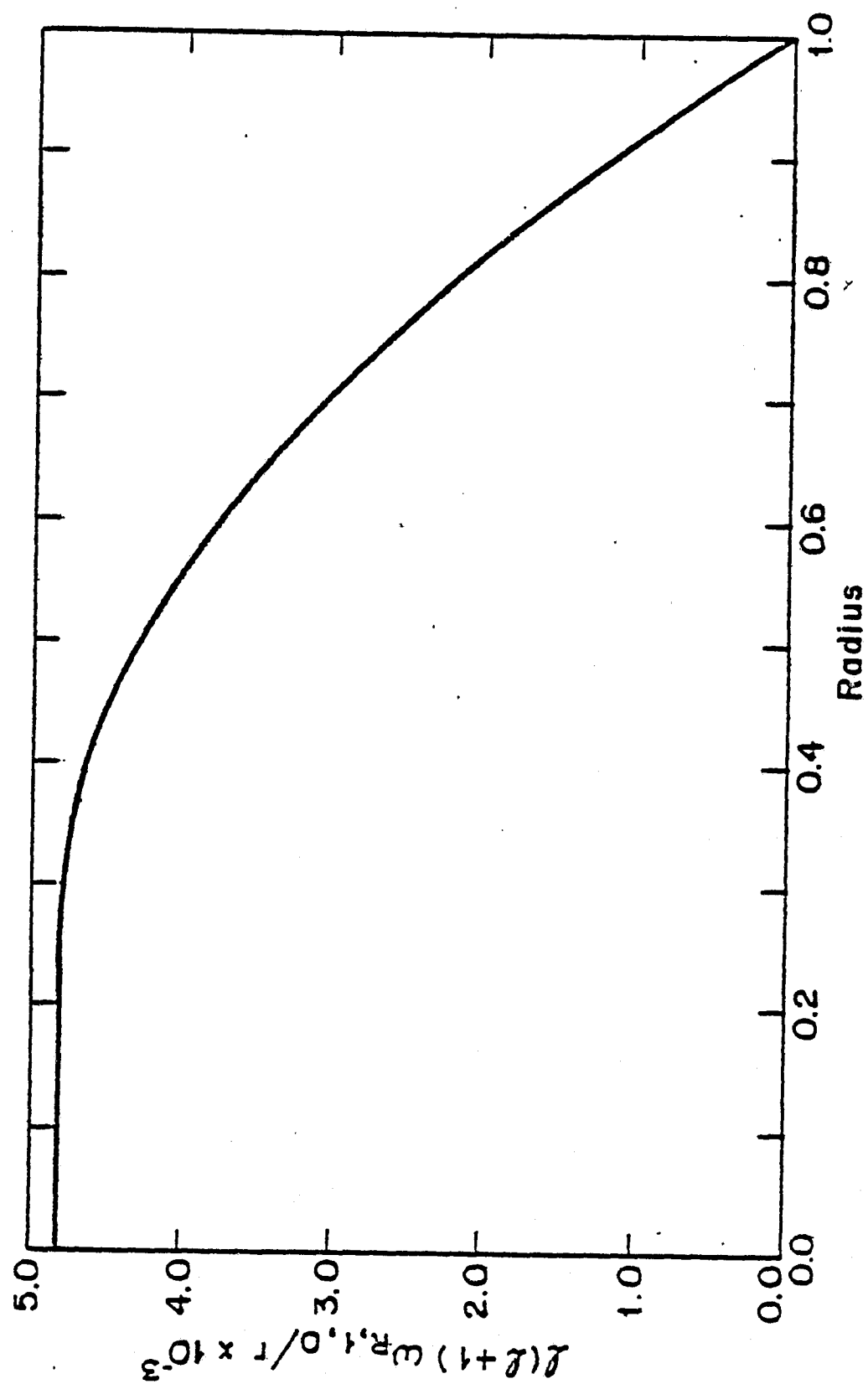
Figure 1

Figure 2
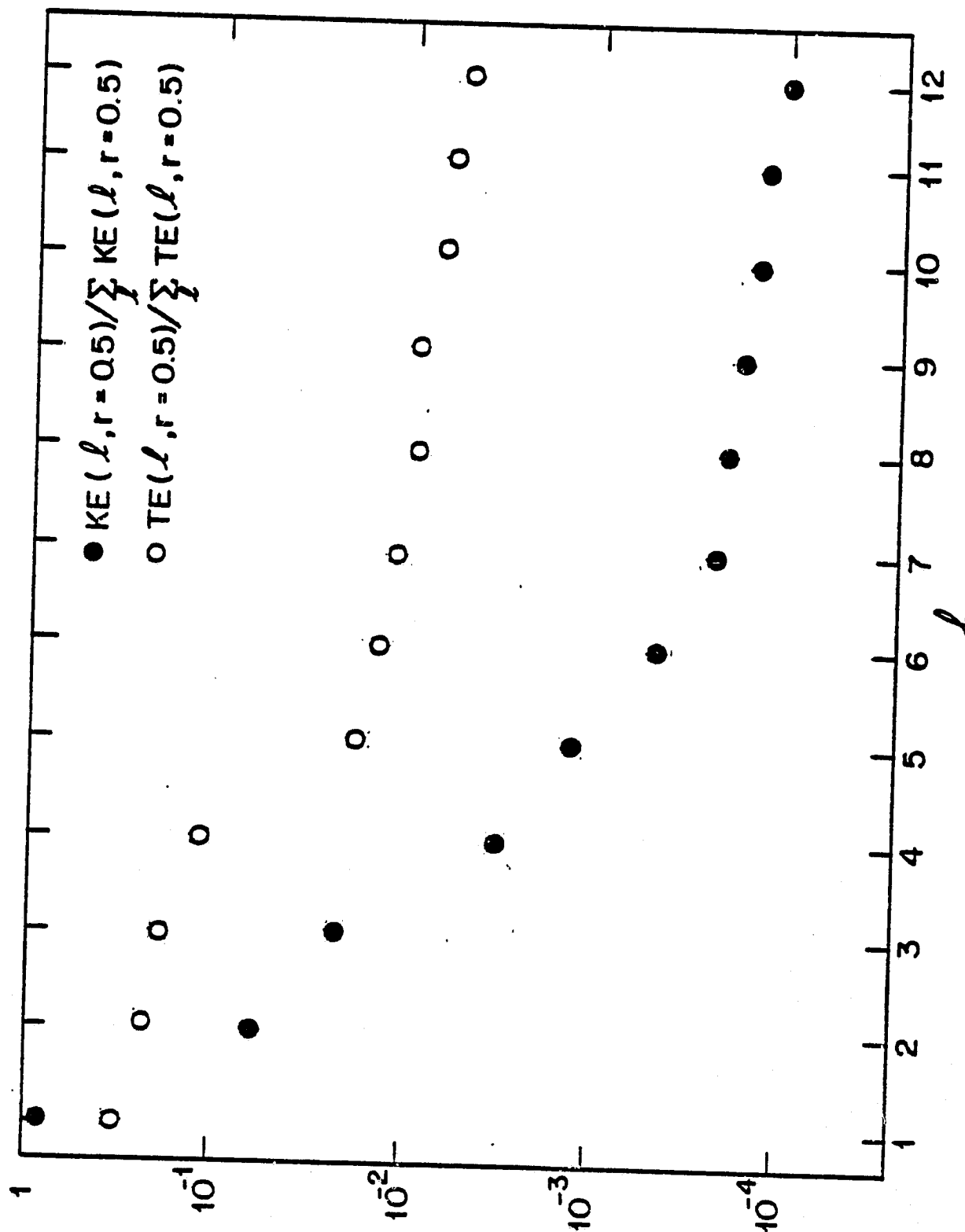
Figure 3
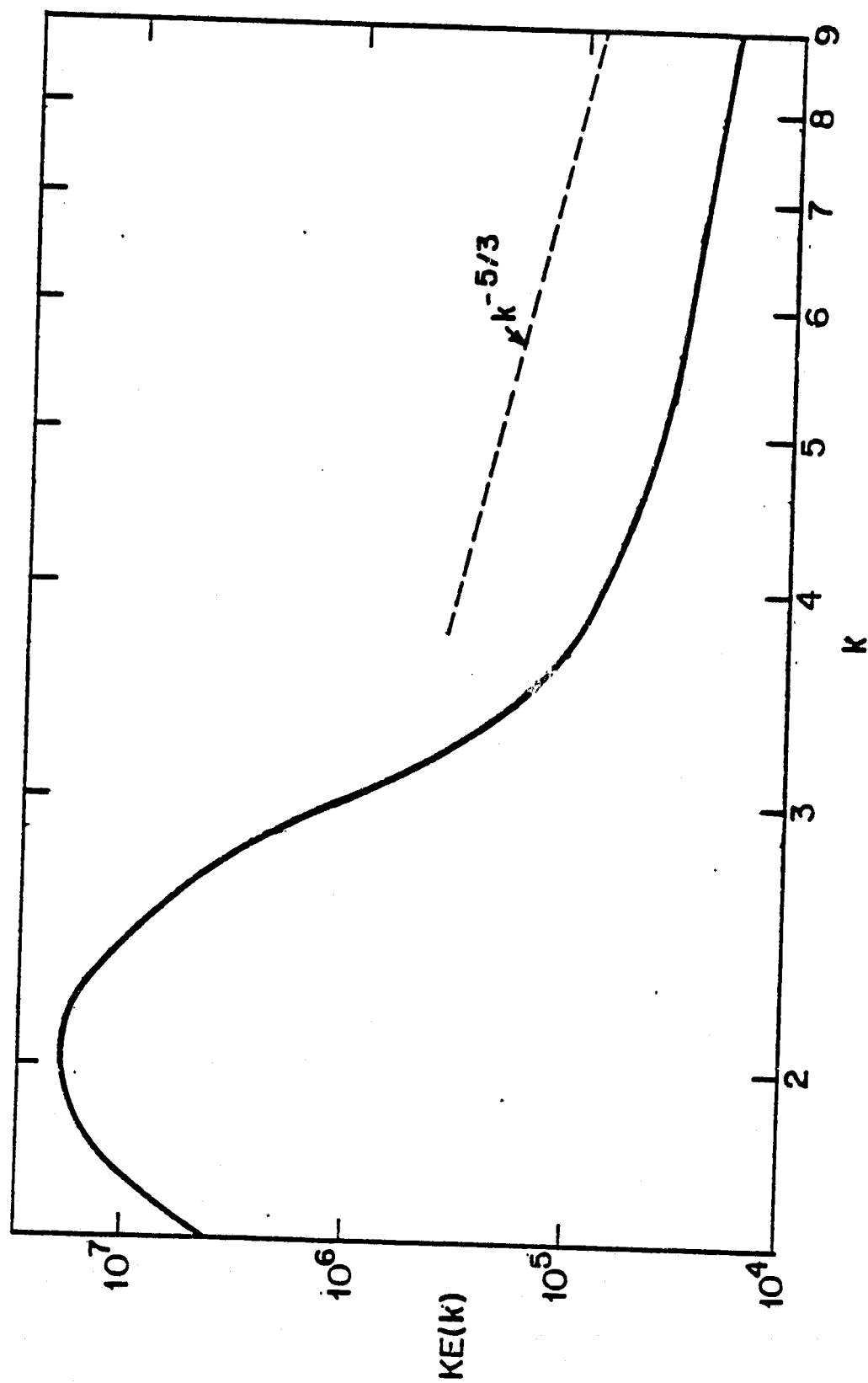
Figure 4
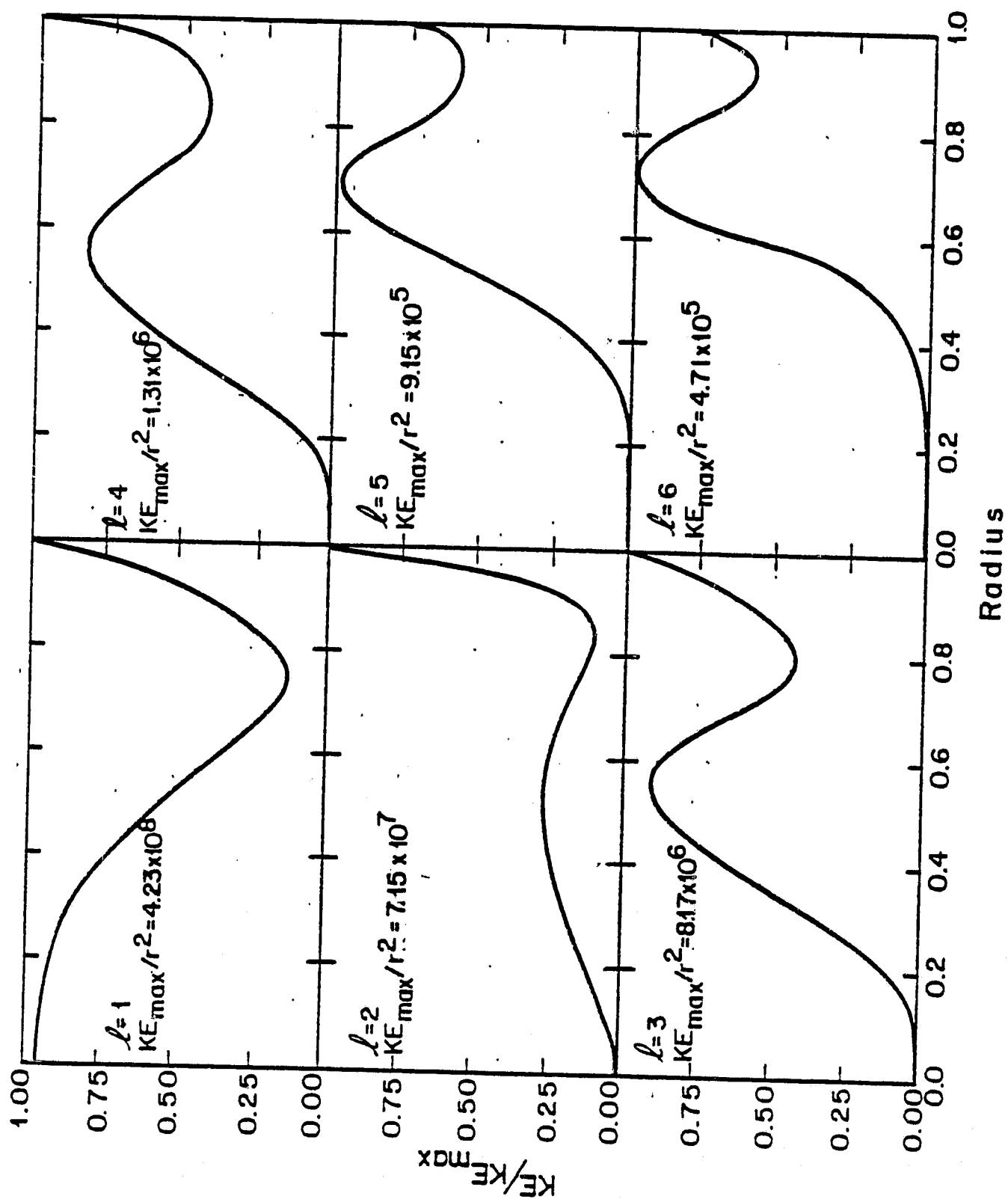
Figure 5a
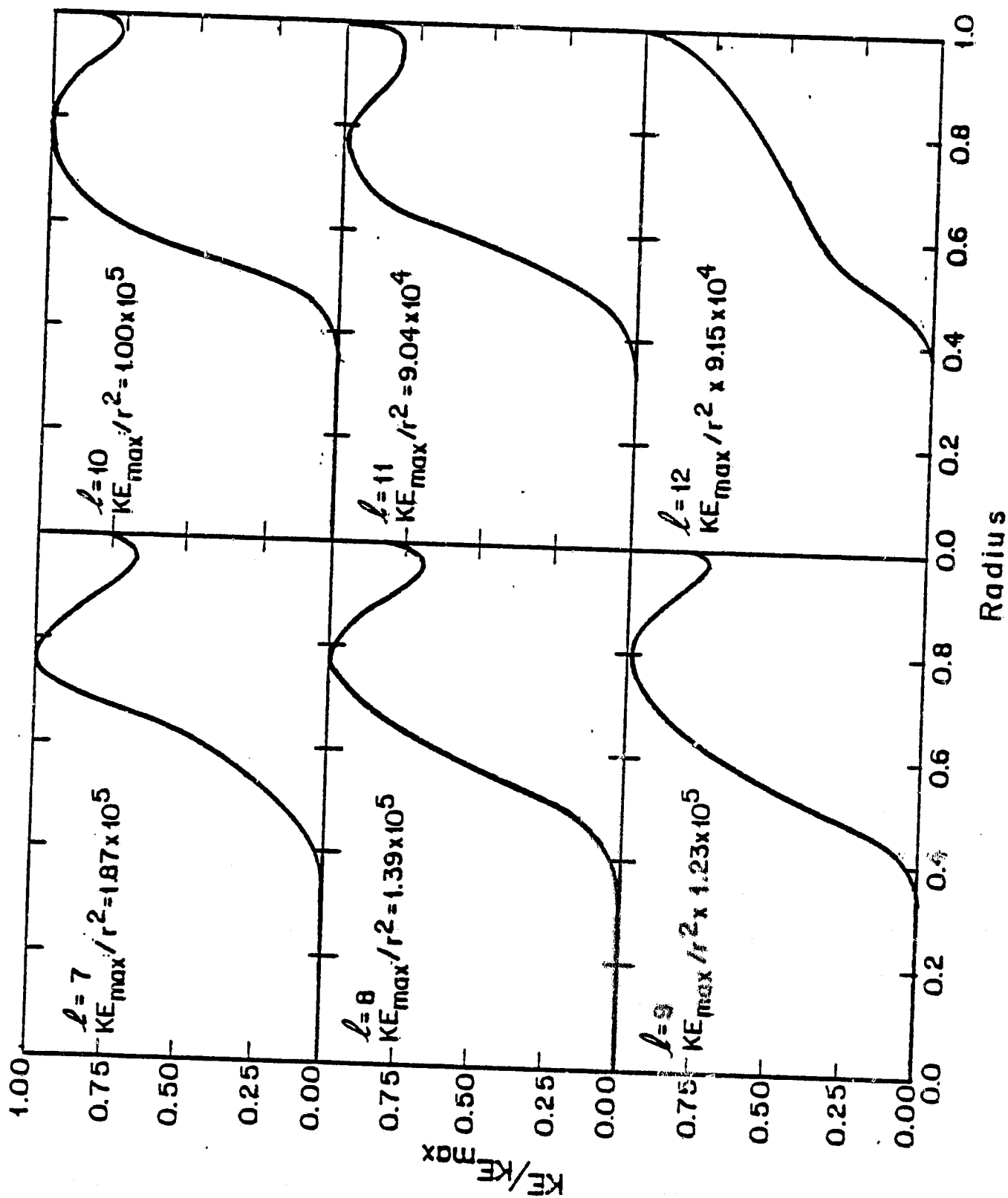
Figure 5b
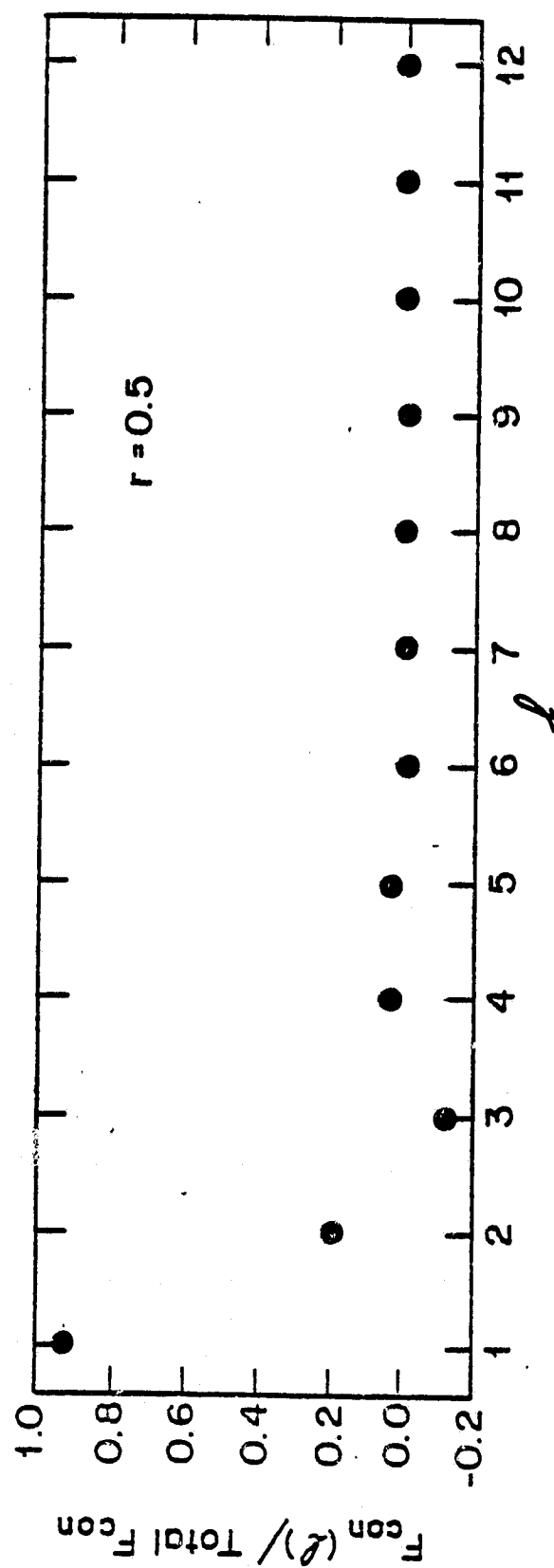
Figure 6

Figure 7

Figure 8a
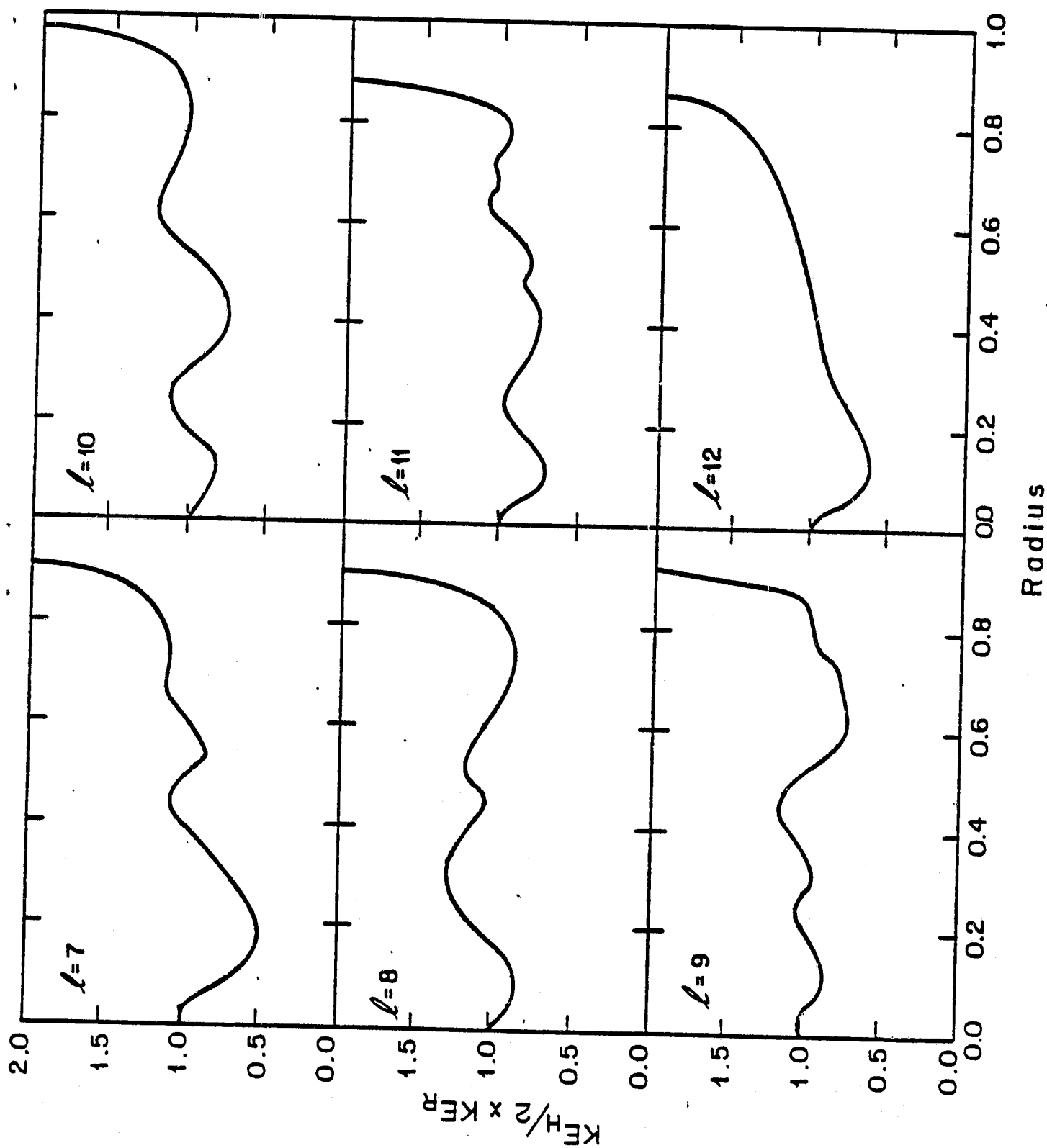
Figure 8b
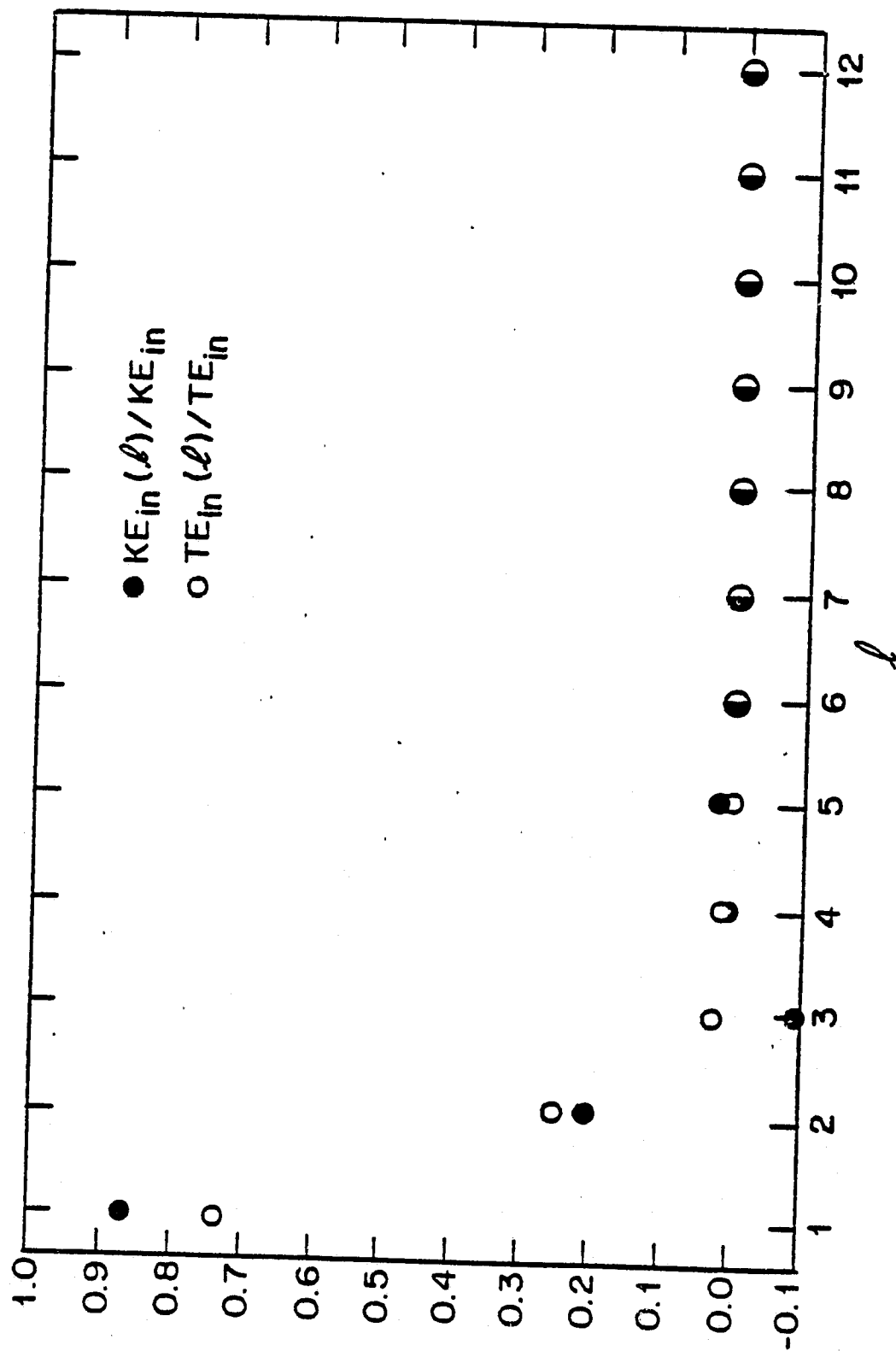
Figure 9

Figure 10

Figure 11
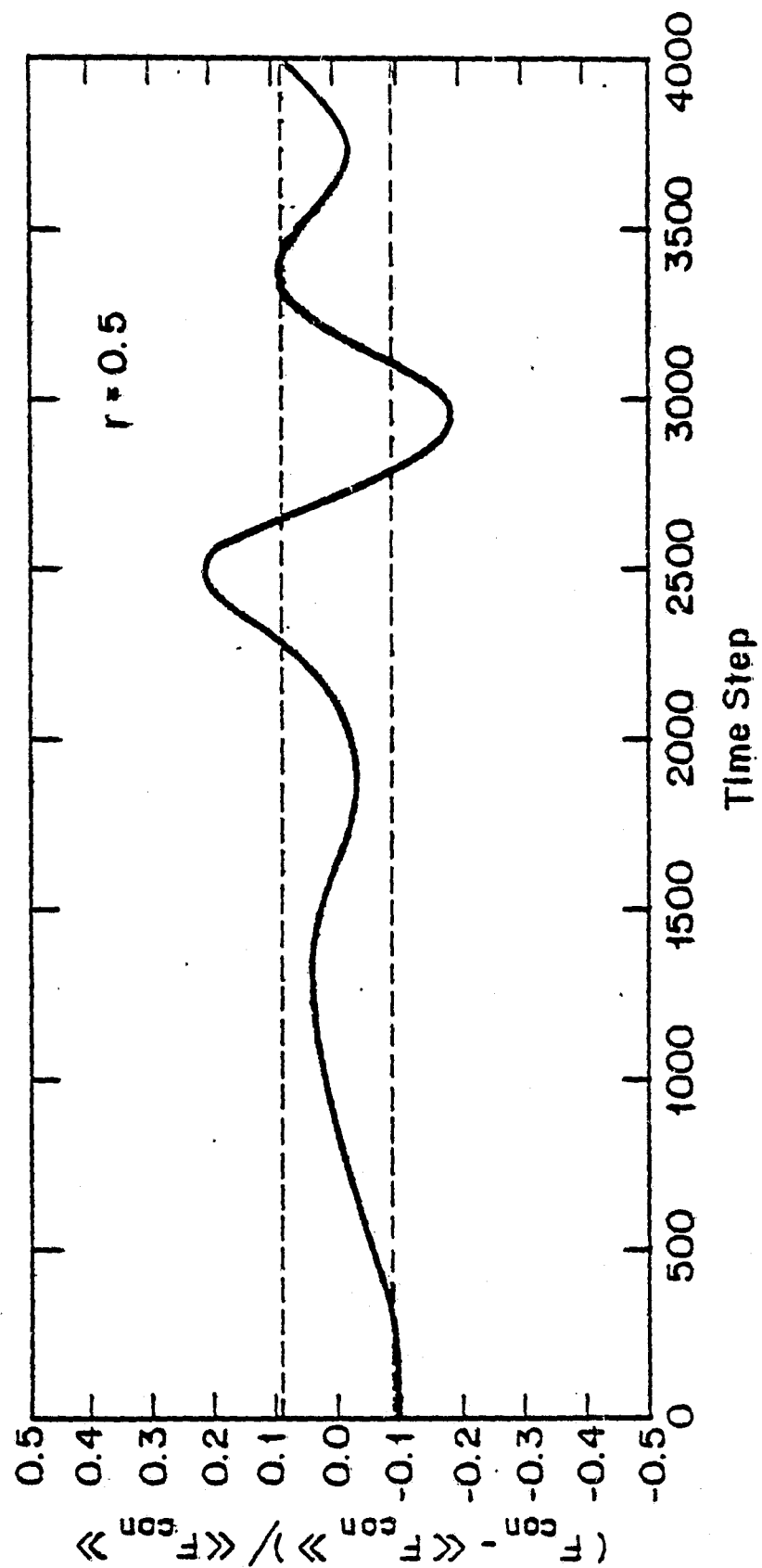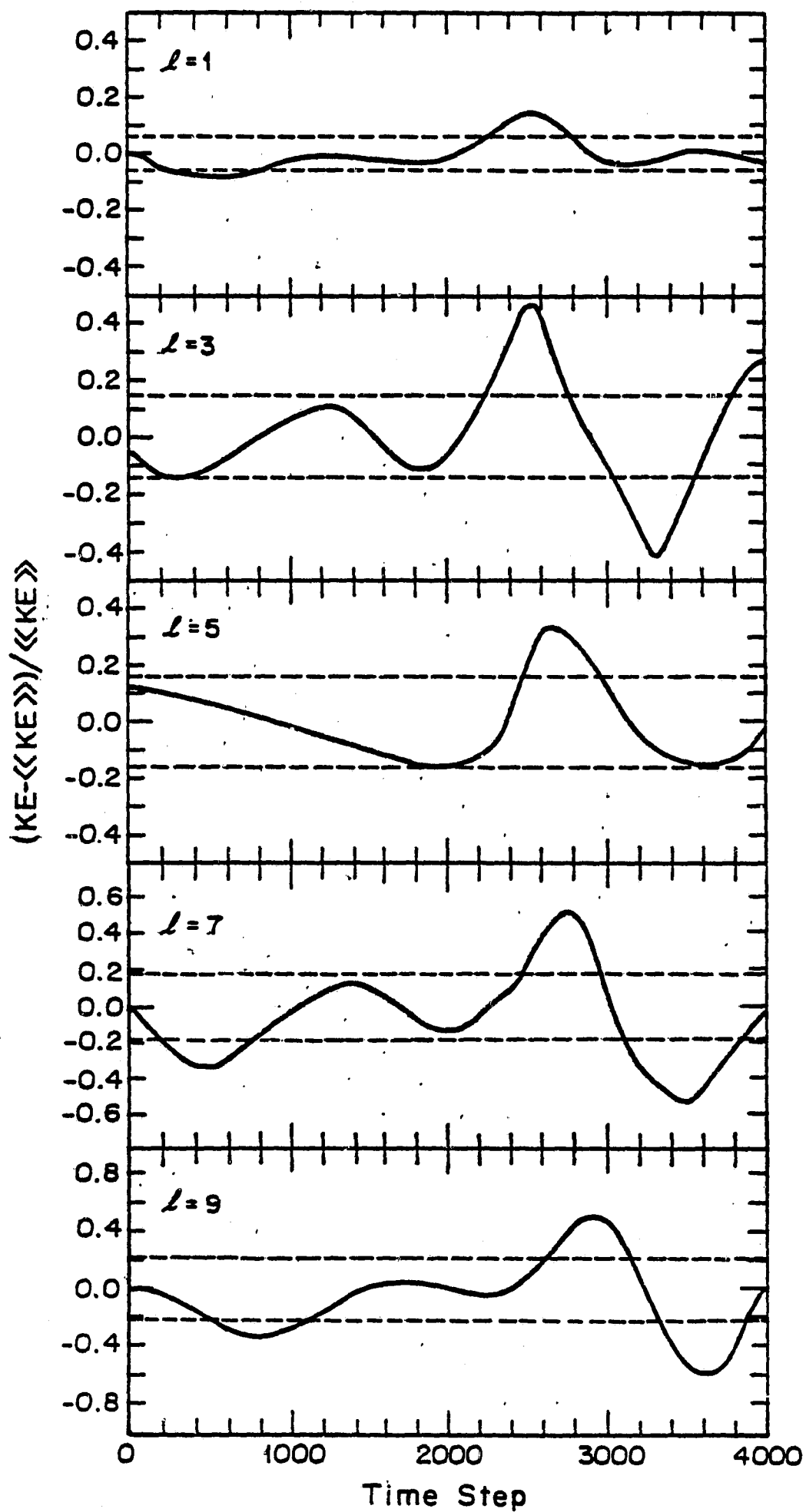
Figure 12

Figure 13
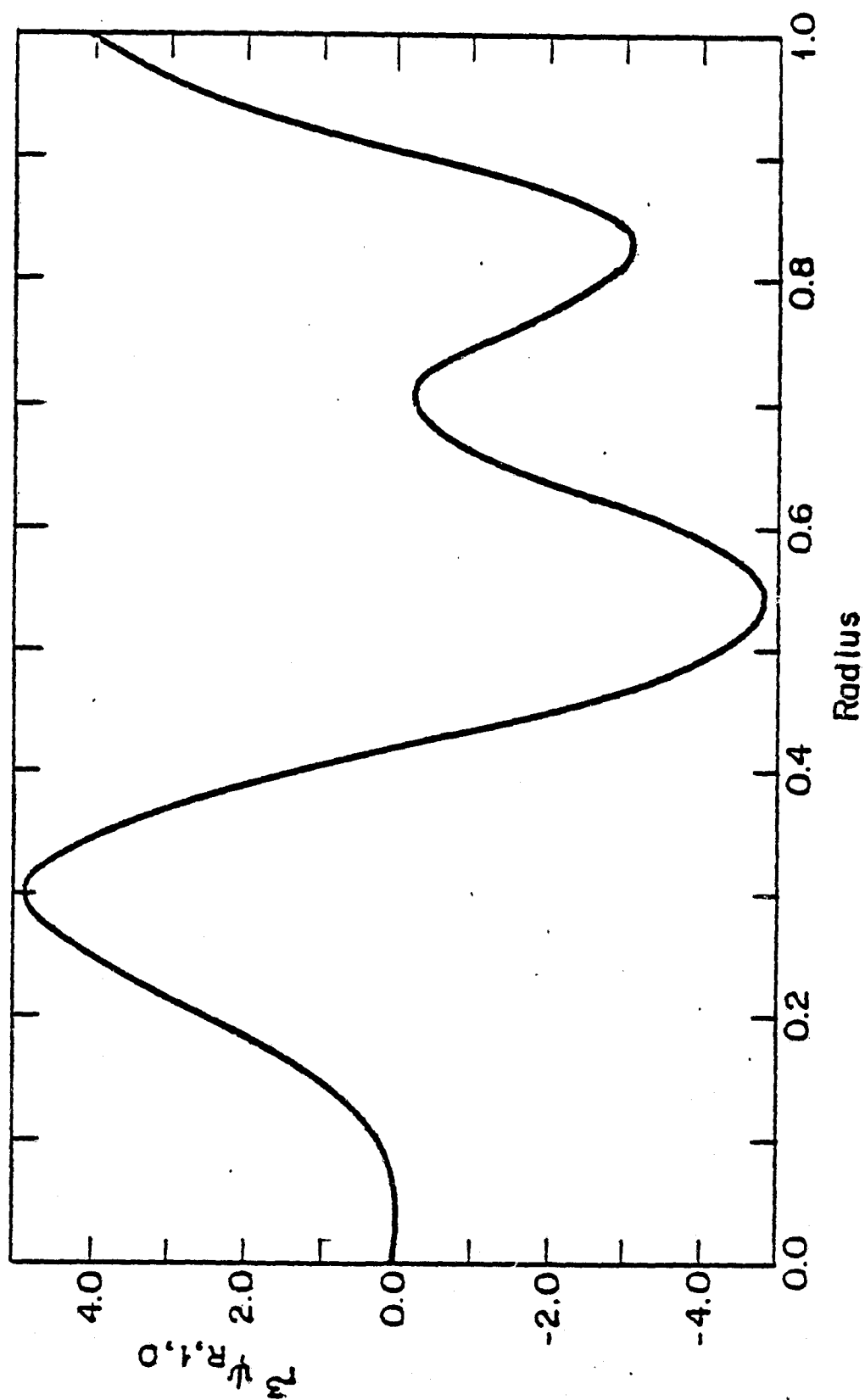
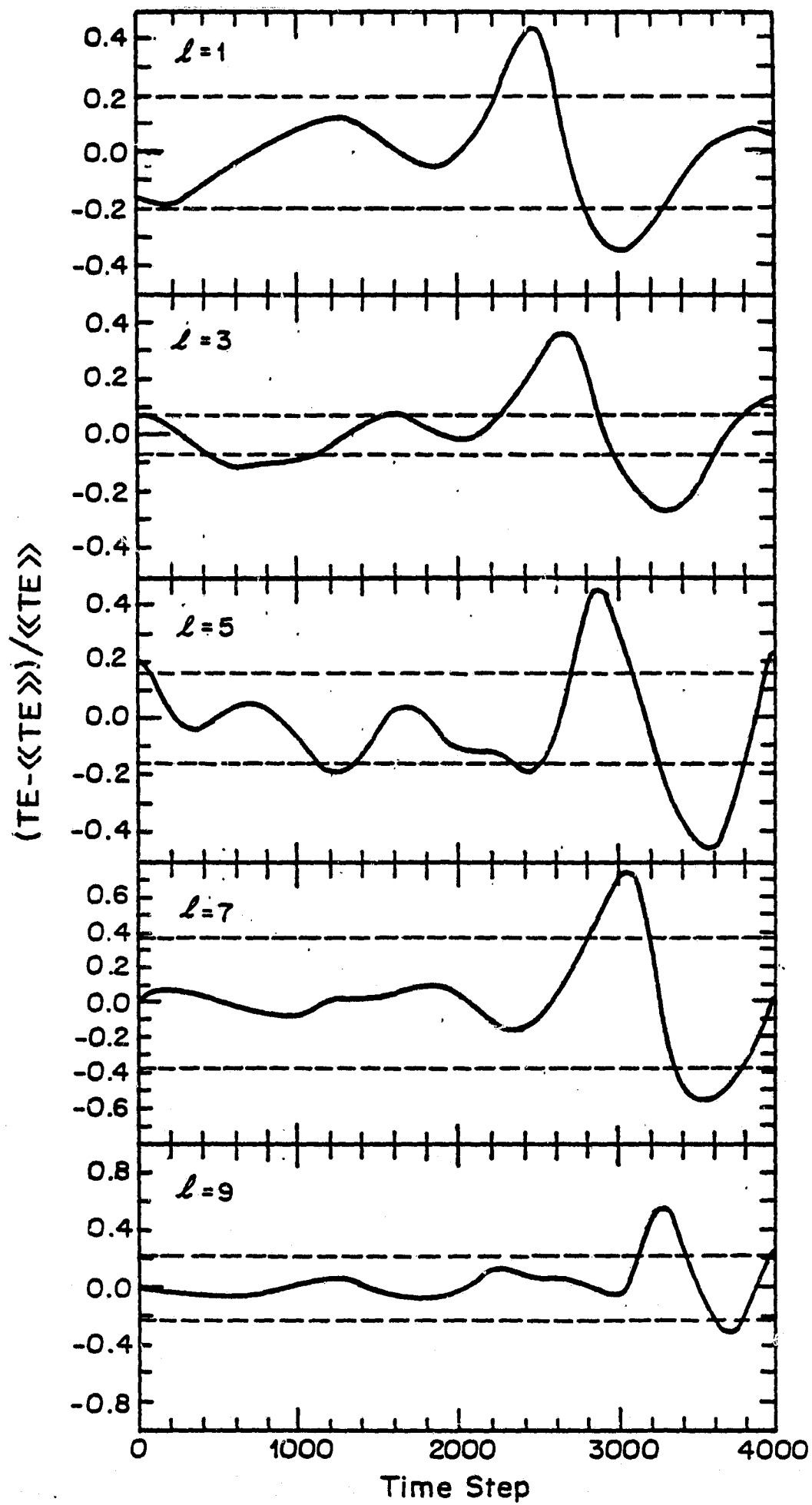Figure 14

Figure 15

Figure 16

Figure 17

AUTHOR'S ADDRESS

PHILIP S. MARCUS

CENTER FOR RADIOPHYSICS

AND SPACE RESEARCH

CORNELL UNIVERSITY

ITHACA, NEW YORK   14853